

# Spin Seebeck Effect: Sensitive Probe for Elementary Excitation, Spin Correlation, Transport, Magnetic Order, and Domains in Solids

Takashi Kikkawa<sup>1</sup> and Eiji Saitoh<sup>1,2,3,4</sup>

<sup>1</sup>Department of Applied Physics, The University of Tokyo, Tokyo 113-8656, Japan; email: t.kikkawa@ap.t.u-tokyo.ac.jp; ORCID: 0000-0002-7789-604X

<sup>2</sup>Institute for AI and Beyond, The University of Tokyo, Tokyo 113-8656, Japan

<sup>3</sup>WPI Advanced Institute for Materials Research, Tohoku University, Sendai 980-8577, Japan

<sup>4</sup>Advanced Science Research Center, Japan Atomic Energy Agency, Tokai 319-1195, Japan

This article is posted with permission from the Annual Review of Condensed Matter Physics, Volume 14 © by Annual Reviews, <http://www.annualreviews.org>.

## Keywords

spin(calori)tronics, antiferromagnetic spintronics, spin Seebeck effect, inverse spin Hall effect, magnon, quantum spin liquid

## Abstract

The spin Seebeck effect (SSE) refers to the generation of a spin current as a result of a temperature gradient in a magnetic material, which can be detected electrically via the inverse spin Hall effect in a metallic contact. Since the discovery of SSE in 2008, intensive studies on SSE have been conducted to elucidate its origin. SSEs appear in a wide range of magnetic materials including ferro-, ferri-, and antiferro-magnets and also paramagnets with classical or quantum spin fluctuation. SSE voltage reflects fundamental properties of a magnet, such as elementary excitation, static magnetic order, spin correlation, and spin transport. In this article, we review recent progress on SSEs in various systems, with particular emphasis on its emerging role as a probe of these magnetic properties in solids. We also briefly discuss the recently-discovered nuclear SSE.

## Contents

1. INTRODUCTION .....	2
2. THEORETICAL ESSENCE OF SPIN SEEBECK EFFECT .....	4
3. SSE AS PROBE OF MAGNON TRANSPORT .....	6
4. SSE AS PROBE OF MAGNETIC ORDER AND DOMAINS .....	8
5. SSE AS PROBE OF SPIN CORRELATION .....	10
6. SSE AS PROBE OF MAGNON POLARIZATION .....	11
7. SSE AS PROBE OF MAGNON-PHONON HYBRIDIZATION AND SCATTERING RATE .....	13
8. SPIN SEEBECK EFFECTS IN QUANTUM MAGNETS .....	16
8.1. Spinons in TL spin liquids .....	16
8.2. Triplons in dimerized spin systems .....	16
8.3. Spin-nematic TL liquids .....	18
9. NUCLEAR-SPIN SEEBECK EFFECT .....	18
10. SUMMARY AND OUTLOOK .....	19

## 1. INTRODUCTION

The spin Seebeck effect (SSE) refers to the generation of a spin current,  $\mathbf{J}_s$ , as a result of a temperature gradient,  $\nabla T$ , in a magnetic material with a metallic contact (1, 2). The effect was first discovered in permalloy in 2008 (3) and later found in electrically insulating yttrium iron garnet (YIG;  $\text{Y}_3\text{Fe}_5\text{O}_{12}$ ) (4) and ferromagnetic semiconductors (GaMnAs) (5) in a configuration where a uniform  $\nabla T$  is applied parallel to the magnetic film plane (Figure 1a). In 2010, the most basic setup called the longitudinal configuration was demonstrated (6), in which  $\nabla T$  across a metal/magnet interface generates a spin current  $\mathbf{J}_s$  along  $\nabla T$  (Figure 1b). In 2015, the nonlocal SSE setup was introduced (Figure 1c) (7), which can be applied to investigate spin-transport properties and further invigorated studies in spin caloritronics (8, 9, 10).

SSE voltages are generated in three steps: (i) the applied  $\nabla T$  excites magnetization dynamics and thereby a magnon spin current (Figure 1d) that (ii) at the interface to the metal becomes a conduction-electron spin current and (iii) is converted into a measurable voltage by the inverse spin Hall effect (ISHE) (11) (Figure 1e). Here, the ISHE is caused by the spin-orbit interaction, which bends electron orbits of up and down spins into opposite directions normal to their velocities. The resultant electric field  $\mathbf{E}_{\text{ISHE}}$  is given by

$$\mathbf{E}_{\text{ISHE}} \propto \theta_{\text{SH}} \mathbf{J}_s \times \hat{\sigma}, \quad 1.$$

where  $\theta_{\text{SH}}$ ,  $\mathbf{J}_s$ , and  $\hat{\sigma}$  are the spin Hall angle, spatial direction of the injected spin current, and unit vector along the electron-spin polarization in the metallic layer (parallel to the equilibrium magnetization  $\mathbf{m}_{\text{eq}}$  of magnet), respectively (Figure 1e) (2). Relatively high voltage is generated in heavy metals such as Pt, Ta, and W due to their large  $\theta_{\text{SH}}$  (11), allowing sensitive detection of SSEs.

The longitudinal configuration (Figure 1b) has been mainly employed in recent studies owing to its simple and straightforward nature (1, 2), enabling systematic and quantitative investigations of SSEs in various magnetic insulators. Note that when a magnetic conductor is used in this configuration, anomalous Nernst effects may overlap with the longitudinal SSE (LSSE) signal (1, 2, 12, 13, 14). Materials used for LSSE measurements are listed

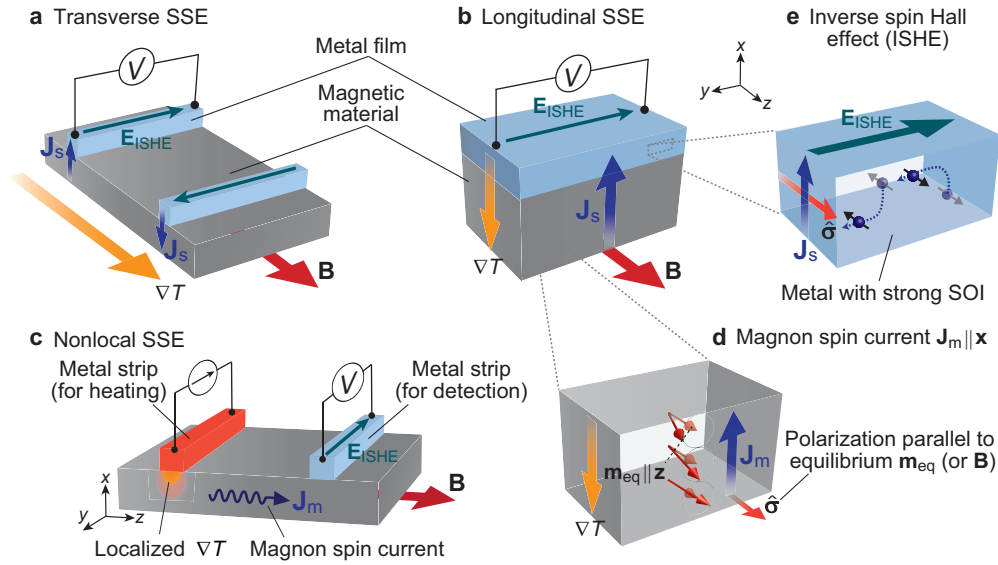


**Figure 1**

Schematic illustrations of the (a) transverse SSE, (b) longitudinal SSE, (c) nonlocal SSE, (d) magnon spin current  $\mathbf{J}_m$ , and (e) inverse spin Hall effect (ISHE).  $\nabla T$ ,  $\mathbf{B}$ ,  $\mathbf{E}_{\text{ISHE}}$ ,  $\mathbf{J}_s$ , and  $\hat{\sigma}$  denote the temperature gradient, external magnetic field (with magnitude  $B$ ), electric field induced by the ISHE (with magnitude  $E_{\text{ISHE}}$ ), spatial direction of the thermally generated spin current, and spin polarization direction of the spin current (parallel to the equilibrium magnetization  $\mathbf{m}_{\text{eq}}$  of the magnetic layer), respectively. In the presence of the strong spin-orbit interaction (SOI), the spin current  $\mathbf{J}_s$  flowing in the metal layer is converted into a transverse voltage via the ISHE.

in Figure 2 in the previous review article (2). Recent updates include ferromagnetic EuO (15), two-dimensional (2D) ferromagnetic  $\text{Cr}_2\text{Si}_2\text{Te}_6$ ,  $\text{Cr}_2\text{Ge}_2\text{Te}_6$  (16, 17), ferrimagnetic garnet ferrites  $R_3\text{Fe}_5\text{O}_{12}$  ( $R = \text{Eu}, \text{Tb}, \text{Dy}, \text{Tm}$ ) (18, 19, 20),  $\text{Y}_{3-x}\text{R}_x\text{Fe}_5\text{O}_{12}$  with  $R$  being 14 rare-earth elements from La to Lu (except for Pm) (21),  $\text{Lu}_2\text{Bi}_1\text{Fe}_4\text{Ga}_1\text{O}_{12}$  (22), spinel ferrites  $\text{ZnFe}_2\text{O}_4$  (23),  $\gamma\text{-Fe}_2\text{O}_3$  (24),  $\text{LiFe}_5\text{O}_8$  (25),  $\text{Ni}_{0.65}\text{Zn}_{0.35}\text{Al}_{0.8}\text{Fe}_{1.2}\text{O}_4$  (26),  $\text{Mg}_{0.5-\delta}\text{Mn}_{0.5}\text{Fe}_2\text{O}_4$  (27), Y-type hexagonal ferrites  $\text{Ba}_2\text{Co}_2\text{Fe}_{12}\text{O}_{22}$ ,  $\text{Ba}_2\text{Zn}_2\text{Fe}_{12}\text{O}_{22}$  (28), orthorhombic ferrimagnetic  $\varepsilon\text{-Fe}_2\text{O}_3$  (29), molecular-based ferrimagnetic  $\text{Cr}^{\text{II}}[\text{Cr}^{\text{III}}(\text{CN})_6]$  (30), various antiferromagnetic (AF) insulators such as NiO (31, 32, 33, 34),  $\text{FeF}_2$  (35),  $\alpha\text{-Fe}_2\text{O}_3$  (36, 37),  $\text{MnCO}_3$  (38),  $\alpha\text{-Cu}_2\text{V}_2\text{O}_7$  (39),  $\text{SrFeO}_3$  (40),  $\text{SrMnO}_3$  (41),  $\text{DyFeO}_3$  (42), and other intriguing materials including a chiral helimagnet  $\text{Cu}_2\text{OSeO}_3$  with a skyrmion lattice phase (43, 44) and quantum magnets  $\text{Sr}_2\text{CuO}_3$  (45, 46),  $\text{CuGeO}_3$  (47),  $\text{Pb}_2\text{V}_3\text{O}_9$  (48),  $\text{LiCuVO}_4$  (49). In particular, the ferrimagnetic insulator YIG has been essential (1, 2), as it exhibits the lowest magnetic damping, high Curie temperature ( $T_C \sim 560$  K), and high resistivity and also is a playground to reveal the role of magnon polarization in SSEs (see Section 6). Experimental reports include temperature  $T$  (50, 51, 52, 53, 54), magnetic field  $B$  (51, 52, 53, 55, 56, 57, 58, 59, 60, 61), length-scale (thickness) (51, 52, 53, 62, 63, 64, 65), structural (66, 67), and time (68, 69, 70, 71, 72, 73, 74) dependence measurements, investigation of the reciprocal effect (75, 76, 77), evaluation of a magnon temperature and chemical potential (78, 79, 80, 81), and so on. Some of the basic experimental results on LSSE for YIG (not focused here) are reviewed in References (1, 2), and we would like to

ask interested readers to consult them.

SSE has been established as a universal phenomenon of magnetic materials, and recently received a lot of attention as a spectroscopic and tabletop tool to detect static and dynamical properties of magnets. In this article, we review recent progress on SSEs in various systems, with emphasis on its emerging role as a probe of elementary excitation, spin correlation, transport and associated scattering rates, static magnetic order and domains in solids. We start with a brief introduction to the mechanism of SSE in Section 2. From Sections 3 to 8, we discuss SSE as a probe for dynamical and static properties of magnetic materials including paramagnets with classical or quantum spin fluctuation. In Section 9, we discuss the SSE driven by nuclear spins. Finally, we conclude this article and provide an outlook for further research opportunities.

## 2. THEORETICAL ESSENCE OF SPIN SEEBECK EFFECT

A theoretical formulation of the magnon-driven SSE was developed by Xiao et al. in 2010 (82). Let us first consider a ferromagnetic insulator (FI) at thermal equilibrium with an attached nonmagnetic metal (NM) (see **Figure 2a**). When the FI is thermally excited, the dynamics of magnetization  $\mathbf{M}(t)$  (with unit vector  $\mathbf{m}(t)$ ) injects a dc spin current into the NM due to spin pumping (11),

$$\langle \mathbf{J}_s^{\text{pump}} \rangle_z = \frac{\hbar g_r^{\uparrow\downarrow}}{4\pi} \langle \mathbf{m} \times \dot{\mathbf{m}} \rangle_z, \quad 2.$$

which is proportional to the real part of the interfacial spin-mixing conductance  $g_r^{\uparrow\downarrow}$  and equal-time and space spin correlation functions or transverse dynamical susceptibility of the FI at the interface (82, 83). At finite temperatures, however, thermal (Johnson–Nyquist) noise in the NM generates a backflow spin current  $\langle \mathbf{J}_s^{\text{back}} \rangle_z$ , which compensates for the pumped spin current  $\langle \mathbf{J}_s^{\text{pump}} \rangle_z$  on average at thermal equilibrium, satisfying the second law of thermodynamics (8). The fluctuation-dissipation theorem shows that the thermal spin current  $\langle \mathbf{J}_s^{\text{pump}} \rangle_z$  from FI to NM ( $\langle \mathbf{J}_s^{\text{back}} \rangle_z$  from NM to FI) is in proportion to the effective magnon (electron) temperature  $T_m$  ( $T_e$ ) in the FI (NM), leading to the net dc component (4, 82)

$$J_s^{\text{int}} = \langle \mathbf{J}_s^{\text{pump}} \rangle_z - \langle \mathbf{J}_s^{\text{back}} \rangle_z = 2\alpha^{(1)} k_B (T_m - T_e), \quad 3.$$

where  $\alpha^{(1)}$  ( $\propto g_r^{\uparrow\downarrow}$ ) is the enhanced damping due to spin pumping. This equation shows that a finite interfacial spin current  $J_s^{\text{int}}$  is generated when an effective magnon-electron temperature difference is induced by an external temperature gradient. Adachi et al. also derived a similar expression by linear response theory (84, 85).

A perturbative treatment of the exchange coupling at the interface is also applied to describe the interfacial SSE (86). Here, conduction electrons in the NM are coupled to the magnetic moments  $\mathbf{m}$  in the FI via exchange interaction, of which the Hamiltonian is written in terms of the creation (annihilation) operators  $a_{\mathbf{q}}^{\dagger}$  ( $a_{\mathbf{q}}$ ) for Holstein-Primakoff magnons and  $c_{\mathbf{k},\sigma}^{\dagger}$  ( $c_{\mathbf{k},\sigma}$ ) for conduction electrons (86):

$$\mathcal{H}_{\text{int}} = \sum_{\mathbf{q}\mathbf{k}\mathbf{k}'} V_{\mathbf{q}\mathbf{k}\mathbf{k}'} a_{\mathbf{q}} c_{\mathbf{k}',\uparrow}^{\dagger} c_{\mathbf{k},\downarrow} + \text{H.c.}, \quad 4.$$

where  $\sigma = \uparrow (\downarrow)$  denotes the electron spin pointing along the  $+z$  ( $-z$ ) direction (see **Figure 2b**). Calculation of the spin-flip rate at the interface based on Fermi's Golden Rule leads

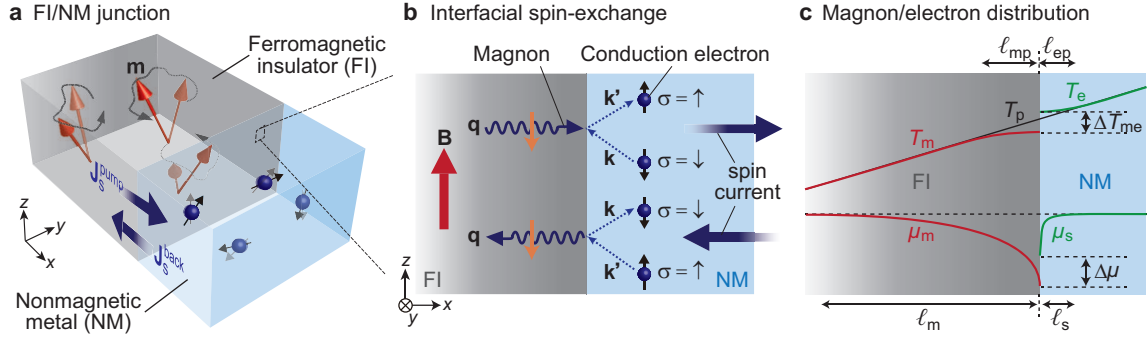


**Figure 2**

(a) FI/NM hybrid structure and spin-pumping current  $\mathbf{J}_s^{\text{pump}}$  (backflow spin current  $\mathbf{J}_s^{\text{back}}$ ) driven by thermal activation of the magnetization  $\mathbf{m}$  in FI (electron spins in NM). At thermal equilibrium,  $\mathbf{J}_s^{\text{pump}}$  and  $\mathbf{J}_s^{\text{back}}$  compensate (82). (b) Interfacial spin-exchange coupling between FI and NM. An electron in NM undergoes a spin-flip inelastic scattering at the interface, creating or annihilating a magnon in FI, which causes an interfacial spin current,  $J_s^{\text{int}}$  (86). (c) A schematic profile of the magnon temperature  $T_m$ , electron temperature  $T_e$ , magnon chemical potential  $\mu_m$ , and electron spin accumulation  $\mu_s$ , assuming a constant phonon temperature gradient  $\nabla T_p$  and disregarding the interfacial heat (Kapitza) resistance.  $T_m$  ( $T_e$ ) and  $\mu_m$  ( $\mu_s$ ) relax on length scales  $\ell_{mp}$  ( $\ell_{ep}$ ) and  $\ell_m$  ( $\ell_s$ ), respectively, which are governed by heat and magnon (spin) diffusion equations (79). For YIG/Pt at room temperature, these length scales are typically  $\ell_{mp}^{\text{YIG}} \sim$  of the order of a nm,  $\ell_m^{\text{Pt}} \sim 10 \mu\text{m}$ ,  $\ell_{ep}^{\text{Pt}} \sim 5 \text{nm}$ , and  $\ell_s^{\text{Pt}} \sim 2 \text{nm}$  (79).

to the interfacial spin current per interfacial area  $A$  ( $J_s^{\text{int}} = A^{-1} \langle ds_z/dt \rangle$ )

$$J_s^{\text{int}} = -\frac{g_r^{\uparrow\downarrow}}{\pi s} \int_{\epsilon_0}^{\infty} d\epsilon \mathcal{D}(\epsilon) (\epsilon - \mu_s) [f_{\text{BE}}(\epsilon, \mu_m, T_m) - f_{\text{BE}}(\epsilon, \mu_s, T_e)], \quad 5$$

where  $s = S/a_0^3$  is the equilibrium spin density of the FI with  $S$  being the total spin in a unit cell with volume  $a_0^3$ . Here,

$$f_{\text{BE}}(\epsilon, \mu_{m(s)}, T_{m(e)}) = \left[ \exp\left(\frac{\epsilon - \mu_{m(s)}}{k_B T_{m(e)}}\right) - 1 \right]^{-1} \quad 6$$

is the Bose–Einstein function describing the distribution for magnons (electron spin accumulation) in the FI (NM) that is parameterized by the magnon temperature  $T_m$  and chemical potential  $\mu_m$  (electron temperature  $T_e$  and spin accumulation  $\mu_s$ ) (Figure 2c) (79, 86, 87).  $\mathcal{D}(\epsilon)$  is the density of states of magnons, and given as  $\mathcal{D}(\epsilon) = [4\pi^2(\hbar D_{\text{ex}})^{\frac{3}{2}}]^{-1} \sqrt{\epsilon - \hbar\gamma B}$  for a parabolic dispersion  $\epsilon = \hbar\omega_{\mathbf{k}} = \hbar D_{\text{ex}} \mathbf{k}^2 + \hbar\gamma B$  ( $D_{\text{ex}}$ : exchange stiffness,  $\gamma$ : electron gyromagnetic ratio). The first (second) term  $\propto \int d\epsilon \mathcal{D}(\epsilon) (\epsilon - \mu_s) f_{\text{BE}}(\epsilon, \mu_m, T_m)$  ( $\propto \int d\epsilon \mathcal{D}(\epsilon) (\epsilon - \mu_s) f_{\text{BE}}(\epsilon, \mu_s, T_e)$ ) in Equation 5 represents the spin-pumping (backflow) contribution from the FI (NM) due to the thermal fluctuation of magnetization (itinerant electron spins) (87), as schematically shown in Figure 2a.  $\mu_m$  in Equation 6 parametrizes magnon accumulation and/or depletion states that cannot be expressed solely by a local  $T_m$  (79). Cornelissen et al. (79) showed that, under the reasonable assumptions that magnons thermalize well with phonons and also that magnon-number conserving scatterings are stronger than magnon-number *non*-conserving scatterings, or magnon decay scatterings characterized by Gilbert damping  $\alpha$ , the introduction of  $\mu_m$  in magnon distribution may give a better explanation for magnon transport phenomena in terms of the length scale (see

**Figure 2c** and Section 3). In linear response, Equation 5 yields

$$\mathbf{J}_s^{\text{int}} = \frac{\sigma_s^{\text{int}}}{\hbar\Lambda}(\mu_s - \mu_m) + \frac{L_{\text{SSE}}^{\text{int}}}{\Lambda}(T_e - T_m), \quad 7.$$

where  $\sigma_s^{\text{int}} = 3\zeta(3/2)\hbar g_r^{\uparrow\downarrow}/2\pi s\Lambda^2$  is the interfacial spin conductivity and  $L_{\text{SSE}}^{\text{int}} = 15\zeta(5/2)k_B g_r^{\uparrow\downarrow}/4\pi s\Lambda^2$  is the interfacial spin Seebeck coefficient with  $\Lambda = \sqrt{4\pi\hbar D_{\text{ex}}/k_B T_m}$  being the thermal de Broglie wavelength (79, 87). The above expression agrees with that derived from the stochastic model by Xiao et al. (82).

Bulk magnon transport in FI also affects the interfacial magnon distribution (Equation 6) as it causes a non-equilibrium magnon accumulation and/or depletion at the interface with NM. A diffusive transport picture should be valid when the FI system size is larger than the magnon mean-free path and magnon thermal wavelength (79). In 2012 and 2014, Zhang and Zhang (88) and Rezende et al. (89, 90) pioneered bulk SSE theories based on diffusion equations of magnons. Subsequently, Cornelissen et al. (79) developed a diffusive magnon spin and heat transport theory based on linearized Boltzmann equations and obtained the magnon spin current  $\mathbf{J}_m$  and heat current  $\mathbf{J}_{Q,m}$  densities in FI as

$$\begin{pmatrix} \frac{2e}{\hbar}\mathbf{J}_m \\ \mathbf{J}_{Q,m} \end{pmatrix} = - \begin{pmatrix} \sigma_m & L/T \\ \hbar L/2e & \kappa_m \end{pmatrix} \begin{pmatrix} \nabla\mu_m \\ \nabla T_m \end{pmatrix}, \quad 8.$$

where  $\sigma_m$  is the magnon spin conductivity,  $L$  is the bulk spin Seebeck coefficient, and  $\kappa_m$  is the magnonic heat conductivity (79). Here, the distributions of  $T_m$  and  $\mu_m$  are governed by diffusion equations with characteristic relaxation lengths (see **Figure 2c**), which are linked with the electron spin diffusion equation in NM by the interfacial boundary condition described as Equation 5 (79).

### 3. SSE AS PROBE OF MAGNON TRANSPORT

The magnon transport relevant to SSEs was first investigated through the thickness  $t_{\text{FI}}$  dependence of magnetic layer in the longitudinal configuration (**Figure 1b**), which clarified the role of bulk magnon transport in SSEs. Length-scale evaluation based on a phenomenological model ( $E_{\text{ISHE}} \propto 1 - \exp(-t_{\text{FI}}/\xi)$ ) yields  $\xi \sim 1 \mu\text{m}$  for YIG/Pt systems at room temperature (51, 53) as well as its  $T$ -scaling of  $\xi \propto T^{-1}$  (53). In 2018, Prakash et al. (64) pointed out the existence of two distinct length scales, a magnon spin-diffusion length ( $\ell_m \sim 10 \mu\text{m}$ ) and a magnon energy relaxation length ( $\ell_u \sim 250 \text{nm}$ ), through the analysis of their  $t_{\text{FI}}$  dependent data for YIG/Pt systems by a magnon diffusion model. In 2020, based on optothermal imaging, Daimon et al. (65) reported the spatially resolved LSSE voltage in a single YIG/Pt system with a  $t_{\text{FI}}$  gradient and found that the  $t_{\text{FI}}$  dependence is identical to that for the (reciprocal) spin Peltier effect (SPE), in which  $\ell_m$  is evaluated as  $3.9 \mu\text{m}$ . Systematic  $t_{\text{FI}}$ -dependent LSSE studies are reported also for  $\text{Fe}_3\text{O}_4$  (91, 92), whose magnon diffusion length is evaluated to be several tens nm. Ramos et al. (93) found the enhanced LSSE in multilayered  $[\text{Fe}_3\text{O}_4/\text{Pt}]_n$  by increasing the stacking number  $n$  and explained the result by introducing a length associated with the multilayered structure.

The nonlocal geometry (**Figure 1c**) provides an alternative approach to address the (lateral) transport of thermally excited magnons (7, 79). **Figure 3a** displays a sketch and optical microscope image of a typical nonlocal SSE device, consisting of two NM (= Pt) strips formed on FI (= YIG) that are electrically isolated from each other by a center-to-center distance  $d$  (7). By applying a charge current to one of the NM (injector) strip, due to

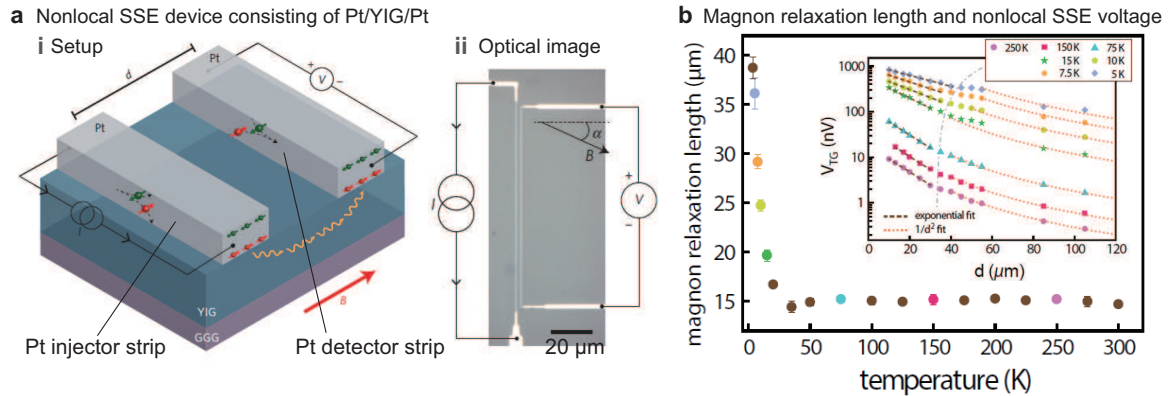


**Figure 3**

(a) (i) Setup for detecting the nonlocal SSE and (ii) optical microscope image for a nonlocal SSE device comprising two Pt injector and detector strips fabricated on an YIG film. Figure reproduced with permission from Reference (7). Copyright © 2015 Springer Nature. (b) Nonlocal SSE voltage  $V_{\text{TG}}$  as a function of  $d$  at various temperatures  $T$  for Pt/YIG/Pt devices (inset) and the magnon relaxation length  $\ell_m$  extracted from exponential fits (main). Figure reproduced with permission from Reference (95). Copyright © 2017 American Physical Society.

its local Joule heating, magnons are thermally excited in the FI layer beneath the strip and diffuse toward the other NM (detector) strip. When a part of them successfully reaches the detector strip, a spin current is injected into the strip and is subsequently converted into an electric voltage by the ISHE. This implies that the distance over which the magnons diffuse is well defined as the separation distance  $d$  (typically,  $d = 500 \text{ nm} \sim 100 \mu\text{m}$ ), allowing us to extract the magnon spin relaxation length  $\ell_m$  via systematic nonlocal SSE measurements as a function of  $d$  (94). A laser heating method is also used to excite magnons, and their diffusion is nonlocally detected in a similar way as described here (97, 98).

The inset to **Figure 3b** shows the nonlocal SSE voltage  $V_{\text{TG}}$  versus  $d$  for Pt/YIG/Pt nanofabricated devices (95).  $V_{\text{TG}}$  monotonically decreases with increasing  $d$ , which corresponds to the decay of the magnon spin signal governed by the magnon spin relaxation length  $\ell_m$  (94). The extracted  $\ell_m$  values increase with decreasing  $T$ , and reach  $\sim 40 \mu\text{m}$  at 3.5 K (**Figure 3b**) (95). The  $\ell_m$  estimation may be affected by the locally distributed  $\nabla T$ , which is discussed in References (95, 96). So far, nonlocal SSEs are reported in several magnets such as ferrimagnetic YIG (94, 95, 96, 97, 98, 99, 100, 101, 102, 103, 104, 105),  $\text{Gd}_3\text{Fe}_5\text{O}_{12}$  (106),  $\text{Tm}_3\text{Fe}_5\text{O}_{12}$  (107),  $\text{NiFe}_2\text{O}_4$  (108),  $\text{MgAl}_{0.5}\text{Fe}_{1.5}\text{O}_4$  (109), antiferromagnetic  $\text{Cr}_2\text{O}_3$  (111, 112),  $\alpha\text{-Fe}_2\text{O}_3$  (37, 110), NiO (34),  $\text{YFeO}_3$  (113),  $\text{BiFeO}_3$  (114), and 2D layered magnets  $\text{MnPS}_3$  (115, 116) and  $\text{CrBr}_3$  (117).

We note that the applied charge current in the injector Pt strip also induces a spin accumulation via the SHE (11) at the interface to YIG, which excites nonequilibrium magnons through the interfacial spin-flip scattering (**Figure 2b**). The electrically-driven magnon flows in YIG, and is finally converted into an ISHE voltage at the detector strip. This all-electrical magnon transport has also been investigated intensively, and recent progress is summarized in Reference (118).

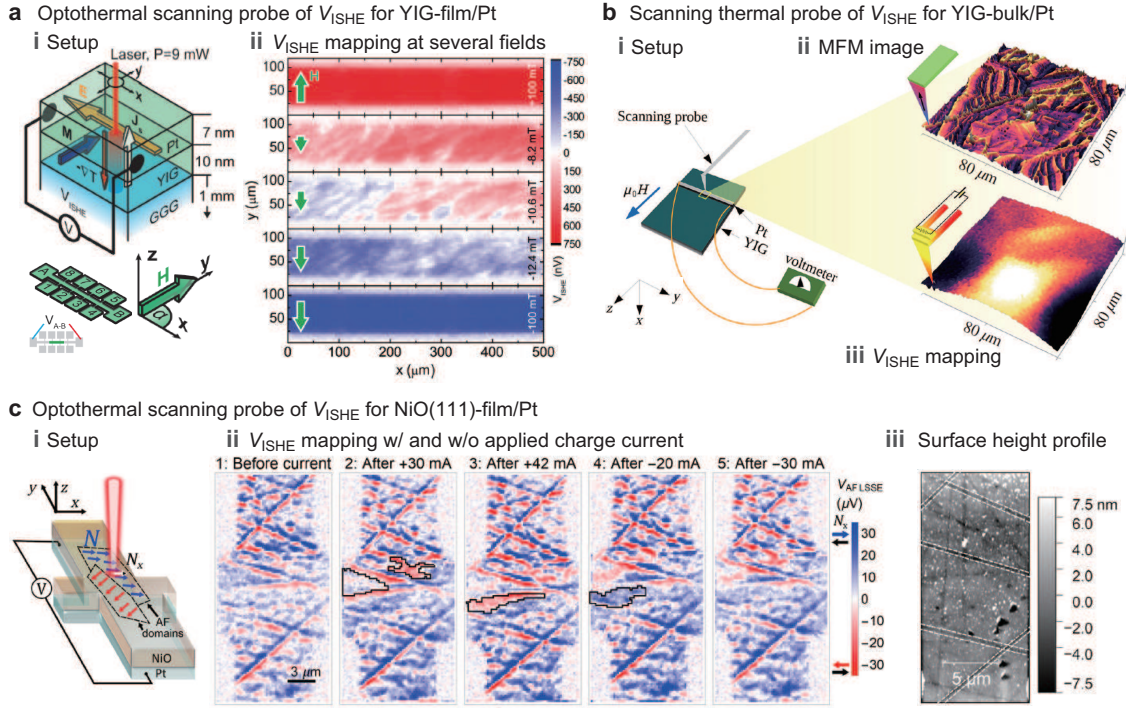


**Figure 4**

(a) (i) Setup for detecting the LSSE in an YIG-film/Pt system with a scannable laser beam. (ii) ISHE voltage  $V_{\text{ISHE}}$  as a function of the laser-spot position  $(x, y)$  at several fields. Figure reproduced with permission from Reference (55). Copyright © 2012 American Physical Society. (b) (i) Setup for detecting the LSSE in an YIG-bulk/Pt system with a scanning thermal probe. (ii) Comparison between the (i) MFM image and (ii)  $V_{\text{ISHE}}$  mapping data. Figure reproduced with permission from Reference (122). Copyright © 2020 American Physical Society. (c) (i) Setup for detecting the LSSE in a NiO(111)-film/Pt system with a scannable laser beam. (ii)  $V_{\text{ISHE}}$  mapping with and without the application of charge current to the Pt film. Blue (red) area represents interfacial spins pointing right (left), some of which are switched with antidamping spin torque (33). Sharp straight lines are attributed to the signal originating from polishing scratches in the MgO (111) substrate that are also visible in the atomic force microscope image shown in (iii). Figure reproduced with permission from Reference (33). Copyright © 2019 Authors, licensed under a Creative Commons Attribution (CC BY) license.

#### 4. SSE AS PROBE OF MAGNETIC ORDER AND DOMAINS

SSE enables electric readout of the magnetic orientation near the magnet/metal interface. This feature is realized by the characteristic of ISHE electric field induced by SSEs:  $\mathbf{E}_{\text{ISHE}} \propto \mathbf{J}_s \times \hat{\sigma}$  (Equation 1) (56, 57). In particular, for LSSEs, the spatial directions of  $\mathbf{J}_s$  and  $\hat{\sigma}$  in NM are, respectively, along the applied  $\nabla T$  and equilibrium magnetization  $\mathbf{m}_{\text{eq}}$  near the interface, meaning that the output field satisfies the relationship  $\mathbf{E}_{\text{ISHE}} \propto \nabla T \times \mathbf{m}_{\text{eq}}$ . The LSSE voltage can therefore extract the projection of the (surface) magnetization on the direction along the magnet/metal interface, allowing to reveal the in-plane magnetic orientation (within  $\ell_m$ ) and also magnetic anisotropies (56, 57, 60, 61, 120, 121).

By utilizing the above feature, magnetic domain structures were detected through LSSE measurements (33, 55, 71, 122). Using a scannable laser beam to create a local  $\nabla T$  on an

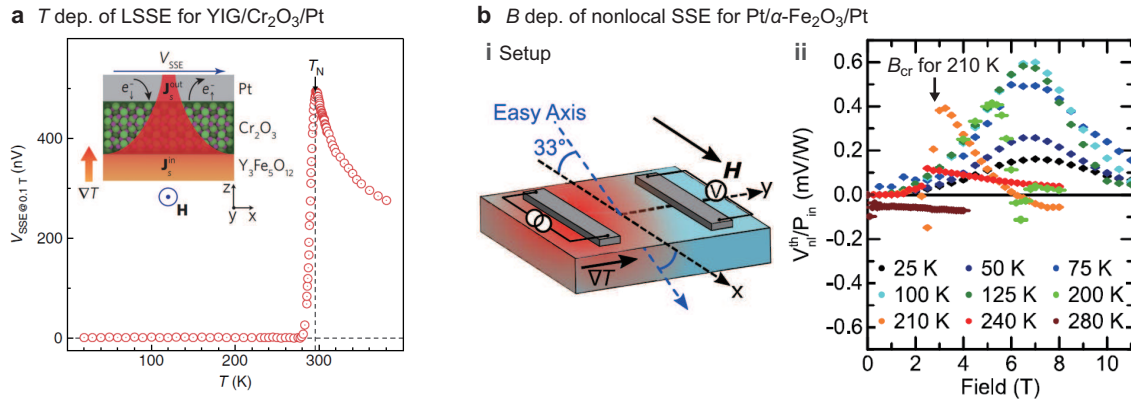


**Figure 5**

(a)  $T$  dependence of the LSSE voltage  $V_{\text{SSE}}$  for an YIG/ $\text{Cr}_2\text{O}_3$ /Pt trilayer (see inset), where the  $c$ -axis of  $\text{Cr}_2\text{O}_3$  is along the out-of-plane direction. With decreasing  $T$ ,  $V_{\text{SSE}}$  sharply drops to zero at  $T_N$  of  $\text{Cr}_2\text{O}_3$ . Figure reproduced with permission from Reference (125). Copyright © 2018 Springer Nature. (b) (i) Setup for a nonlocal SSE for a Pt/ $\alpha$ - $\text{Fe}_2\text{O}_3$ /Pt sample. (ii)  $T$  dependence of the nonlocal voltage normalized by the applied heating power  $V_{\text{nl}}^{\text{th}}/P_{\text{in}}$  at selected  $T$ .  $B_{\text{cr}}$  indicates a critical field at which  $\mathbf{n}$  reorientates perpendicular to  $\mathbf{B}$ . Figure reproduced with permission from Reference (37). Copyright © 2021 American Physical Society.

YIG-film/Pt bilayer, Weiler et al. (55) demonstrated a spatial mapping of in-plane magnetic structure of the YIG (Figure 4a). Bartell et al. (71) extended the approach into the time domain and addressed spatiotemporal thermal evolution of the LSSE in an YIG-film/Pt bilayer with sub-100 ps resolution. Sola et al. (122), instead, used a scanning thermal probe consisting of a micropatterned cantilever and heated up the tip that is in contact with an YIG-bulk/Pt sample to create a local  $\nabla T$ . By scanning the cantilever tip, they observed a spatially resolved voltage response that depends on the magnetic domain distribution confirmed by magnetic force microscopy (MFM) (Figure 4b). In 2019, Gray et al. (33) applied the optothermal imaging method for NiO-film/Pt systems, and obtained AF domain distributions at zero field and room temperature (Figure 4c), where the LSSE signal was attributed to the Néel order contribution. They also successfully visualized the domain rotation and domain wall motion due to the antidamping spin torque induced by the SHE in Pt (Figure 4c, subpanel ii). The technique may provide a simple and versatile way to characterize AF domains and to understand the spin-torque switching in antiferromagnets (AFMs).

We would like to note that thermal imaging of the reciprocal process of SSE (i.e., the SPE (65, 75, 76, 77, 123)) can also sensitively detect the magnetic orientation and domains. In 2018, Yagmur et al. (124) identified the magnetization distributions for ferrimagnetic GdIG across its magnetic compensation temperature  $T_{\text{comp}}$ , at which the reorientation of the sublattice magnetizations of GdIG was observed as the change of the heat-current direction in the SPE.

SSE-based detection of the Néel order and associated dynamics has also been reported through different approaches. In 2018, Qiu et al. (125) observed an on-off switching behavior in the LSSE voltage in YIG/ $\text{Cr}_2\text{O}_3$ /Pt trilayers across the Néel temperature  $T_N = 296$  K (Figure 5a). Here, below  $T_N$ , the Néel vector  $\mathbf{n}$  of  $\text{Cr}_2\text{O}_3$  is pinned to the out-of-plane

direction (easy-axis  $\parallel c$ ) that is orthogonal to the spin component carried by magnons in the in-plane magnetized YIG film. This prohibits magnon transmission from YIG to  $\text{Cr}_2\text{O}_3$ , and thus sharply suppresses the LSSE voltage below  $T_N$ , being responsible for the observation (125). In 2021, Ross et al. (37) demonstrated the nonlocal SSE mediated by the Néel vector  $\mathbf{n}$  in  $\alpha\text{-Fe}_2\text{O}_3$  under the external  $B$  parallel to the easy-axis and the attached metal (Pt) strips (Figure 5b, subpanel *i*), which allows for excluding significant contributions from the net magnetization vector (37). In the easy-axis phase of  $\alpha\text{-Fe}_2\text{O}_3$ , close to but below the Morin transition temperature ( $T_M = 240$  K) such as 210 K, the nonlocal SSE voltage is initially constant around zero at a low  $B$ , but shows a sharp negative dip to positive peak transition across a critical field,  $B_{\text{cr}}$ , where  $\mathbf{n}$  reorientates perpendicular to  $\mathbf{B}$  (Figure 5b, subpanel *ii*). The result may be attributed to fluctuations of the Néel order as the magnetic anisotropy is compensated by the applied  $B$  (37). This work highlights the importance of the Néel-order magnon transport in the nonlocal SSE. We note that AF SSE induced by Néel dynamics is also demonstrated in the longitudinal configuration in  $\alpha\text{-Fe}_2\text{O}_3$  and  $\text{Cr}_2\text{O}_3$  (36, 126, 127), which we discuss in Section 6. In 2021, Luo and Liu et al. (128, 129) reported the LSSE-based detection of interfacial AF spin sublattices in  $\text{Cr}_2\text{O}_3$  and their control by the applied electric field in the spin-flop phase at high magnetic fields, providing a new approach for controlling spin currents in AFMs. Very recently, Parsonnet et al. (114) reported non-volatile electric field control of the nonlocal SSE in multiferroic  $\text{BiFeO}_3$  without external  $B$  via the deterministic control of ferroelectric and magnetic order in  $\text{BiFeO}_3$ .

## 5. SSE AS PROBE OF SPIN CORRELATION

As described in Section 2, in SSE the interfacial spin current is generated by the spin pumping, which indicates that SSE is sensitive to the transverse dynamical susceptibility or spin correlation function (82, 83). To test the concept, a paramagnetic phase just above the magnetic ordering temperature is an intriguing platform, at which the conventional magnon picture is no longer applicable, but short-range correlation of spin fluctuations may exist.

Wu et al. (138, 139) investigated the LSSEs in the paramagnetic phase of  $\text{Gd}_3\text{Ga}_5\text{O}_{12}$  (GGG) and  $\text{DyScO}_3$  (Figure 6a). GGG does not exhibit long-range magnetic ordering down to  $T \ll |\Theta_{\text{CW}}|$  ( $\Theta_{\text{CW}} = -2.3$  K is the Curie-Weiss temperature (138)), but shows signatures of short-range correlations up to at least 5 K.  $\text{DyScO}_3$  is a rather conventional AFM with the low  $T_N$  of 3.1 K. The observed SSE coefficient for GGG follows a scaling close to  $T^{-1}$  as expected from the Curie-Weiss law ( $\chi = C/(T - \Theta_{\text{CW}})$ ). Besides, anisotropic  $B$  dependencies in the LSSE for GGG were observed, and discussed in terms of short-range magnetic order due to geometrical frustration of GGG (139). As a side note, owing to its large  $\text{Gd}^{3+}$  spin of 7/2, GGG may show strong dipolar interaction under high  $B$ , generating collective spin-wave excitations, which may support bulk spin transport in GGG (140).

In 2019, Li et al. (35) reported careful experiments and analysis on the AF LSSE in  $\text{FeF}_2$  around its phase transition temperature ( $T_N = 70$  K). The experimental SSE coefficient near and above  $T_N$  follows the critical scaling law with the critical exponents for magnetic susceptibility of 3D Ising systems, rather than the field-induced sublattice magnetization (Figure 6b). This work clearly demonstrates that SSE is capable of probing correlations of spin fluctuations in magnetic systems (35). In the same year, Yamamoto et al. (141) developed a linear response theory of AF SSE at elevated temperatures, predicting a cusp

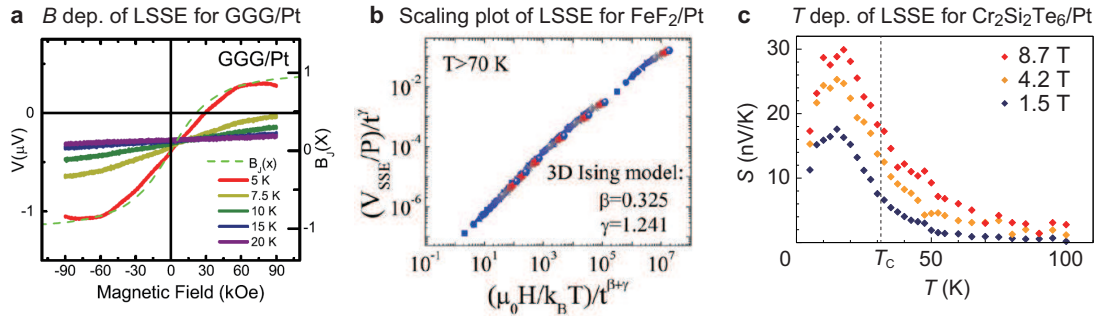


**Figure 6**

(a)  $B$  dependence of the LSSE voltage  $V$  for a  $\text{Gd}_3\text{Ga}_5\text{O}_{12}$ (GGG)/Pt system at selected  $T$  and the Brillouin function  $B_J$  for  $S = 7/2$  at 5 K. Figure reproduced with permission from Reference (138). Copyright © 2015 American Physical Society. (b) Scaling plot of the LSSE for a  $\text{FeF}_2$ /Pt system above  $T = 70$  K.  $V_{\text{SSE}}$ ,  $P$ , and  $t$  represent, respectively, the SSE voltage, applied heating power, and the reduced temperature:  $t = (T - T_N)/T_N$  for  $T > T_N$ . Figure reproduced with permission from Reference (35). Copyright © 2019 American Physical Society. (c)  $T$  dependence of the LSSE voltage  $S = E_{\text{ISHE}}/\nabla T$  for a  $\text{Cr}_2\text{Si}_2\text{Te}_6$ /Pt system at selected  $B$ . Figure reproduced with permission from Reference (16). Copyright © 2019 American Physical Society.

structure at  $T_N$  consistent with the experiment by Li et al. (35).

It is worth mentioning that an insertion of an AF (NiO, CoO) film between FI (YIG) and NM (Pt, Ta, etc.) increases the LSSE signal especially at around  $T_N$ , which is attributed to the enhanced spin conductance in the AF spacer around its  $T_N$  (130, 131, 132). This feature is also seen in an YIG/ $\text{Cr}_2\text{O}_3$ /Pt system at  $T_N = 296$  K of  $\text{Cr}_2\text{O}_3$  (Figure 5a (125)).

Van der Waals 2D materials provide a fertile ground to study the effect of anisotropic spin correlation on SSE. Ito et al. (16) measured LSSEs in 2D layered FIs  $\text{Cr}_2\text{Si}_2\text{Te}_6$  ( $T_C \sim 31$  K) and  $\text{Cr}_2\text{Ge}_2\text{Te}_6$  ( $T_C \sim 65$  K) that exhibit in-plane short-range ferromagnetic correlations up to at least 300 K (200 K) for  $\text{Cr}_2\text{Si}_2\text{Te}_6$  ( $\text{Cr}_2\text{Ge}_2\text{Te}_6$ ), whereas out-of-plane correlations disappear slightly above  $T_C$  (144, 145). The LSSEs turned out to persist above  $T_C$ , but disappear around 50 K (90 K) for a  $\text{Cr}_2\text{Si}_2\text{Te}_6$ /Pt ( $\text{Cr}_2\text{Ge}_2\text{Te}_6$ /Pt) system (Figure 6c). The results show that the in-plane ( $\perp \nabla T$ ) spin correlations do not solely produce the LSSE voltage; spin transport ( $\parallel \nabla T$ ) between the planes enabled by the out-of-plane correlations is important to create nonequilibrium magnon population that leads to a finite interfacial spin current (16).

## 6. SSE AS PROBE OF MAGNON POLARIZATION

A magnon may possess a positive (+) or negative (−) polarization, depending on whether the magnon mode carries a  $+\hbar$ - or  $-\hbar$ -spin angular momentum. In a classical picture, the + (−) polarization corresponds to the counterclockwise (clockwise) rotation of a magnetic moment  $\mathbf{m}$  around the applied field  $\mathbf{B}$  (133). In a ferromagnet, magnons have a single + polarization (Figure 7a, subpanel i), whereas in a uniaxial AFM there are two magnon modes with + and − polarizations that are degenerated at zero field (Figure 7a, subpanel ii). In a ferrimagnet, both + and − polarized magnon modes exist due to the opposite sublattice moments that are split by the exchange field between the sublattices, and the − polarized mode has higher energy than the + one (134).

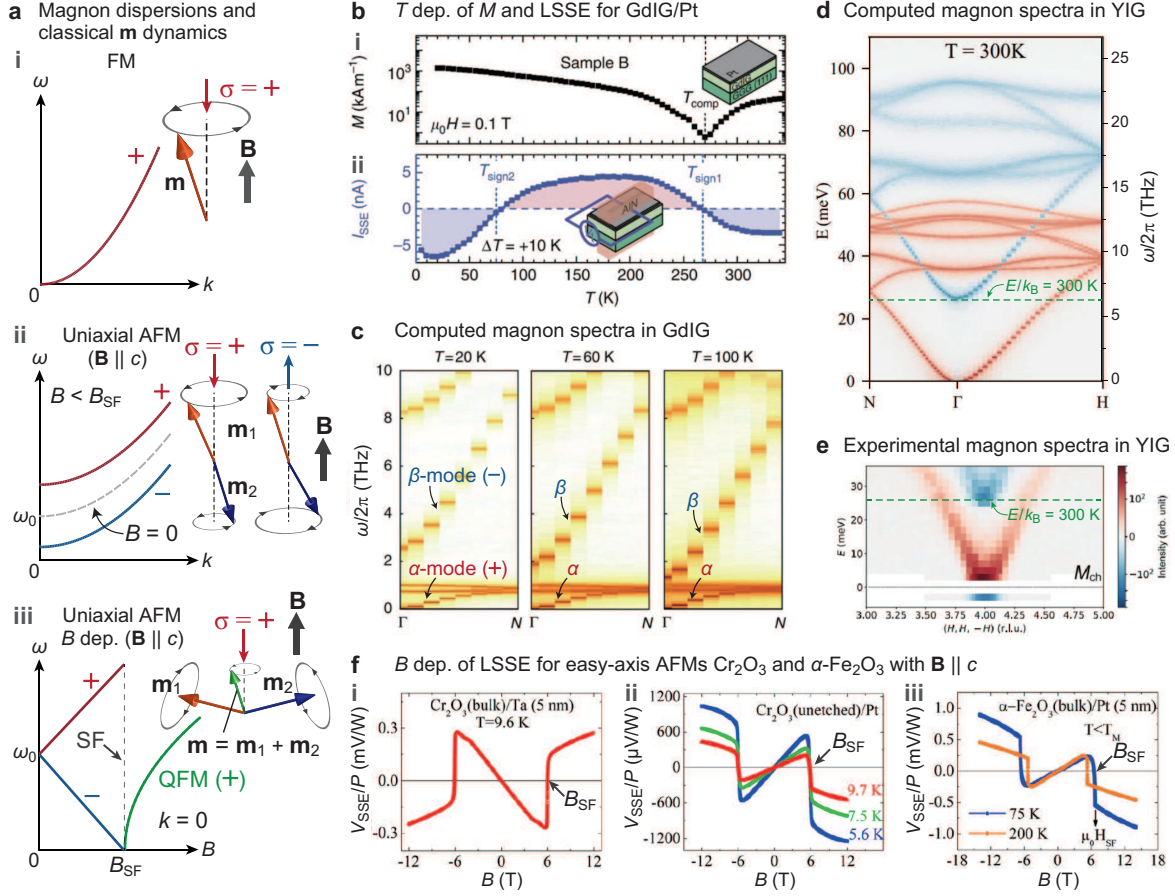


**Figure 7**

(a) Magnon dispersion relations and corresponding magnetization  $\mathbf{m}$  dynamics for (i) a ferromagnet (FM) and (ii) a uniaxial antiferromagnet (AFM) under  $\mathbf{B} \parallel c$  (easy-axis) below the spin-flop (SF) field  $B_{\text{SF}}$ . (iii) Magnon gap at  $k = 0$  versus  $B$  for  $\mathbf{B} \parallel c$ . For  $B > B_{\text{SF}}$ , the quasi-ferromagnetic (QFM) mode appears (36, 126).  $\sigma = + (-)$  represents the positive (negative) magnon polarization. (b)  $T$  dependence of (i)  $M$  in a GdIG film and (ii) the LSSE signal  $I_{\text{SSE}} = V_{\text{SHE}}/R_{\text{Pt}}$  ( $R_{\text{Pt}}$ : Pt resistance). (c) Magnon spectra of GdIG computed with ASD modelling. (b),(c) Figure reproduced with permission from Reference (135). Copyright © 2016 Authors, licensed under a Creative Commons Attribution (CC BY) license. (d),(e) Magnon spectra of YIG at room temperature (d) obtained by implementing a quantum thermostat into ASD modelling and (e) measured with inelastic polarized neutron scattering. Dashed green lines show the thermal energy  $k_{\text{B}}T$  at 300 K. (d) Figure reproduced with permission from Reference (136). Copyright © 2019 American Physical Society. (e) Figure reproduced with permission from Reference (133). Copyright © 2020 American Physical Society. (f)  $B$  ( $\mathbf{B} \parallel c$ ) dependence of the LSSE voltage normalized by the heating power  $V_{\text{SSE}}/P$  for easy-axis AFMs (i, ii)  $\text{Cr}_2\text{O}_3$  and (iii)  $\alpha\text{-Fe}_2\text{O}_3$  below  $T_{\text{M}}$  with metal (Ta, Pt) contacts. Figure reproduced with permission from Reference (36). Copyright © 2020 AIP Publishing.

In 2016, Geprägs et al. (135) showed that SSE can be a measure of the magnon polarization. They observed two sign changes in the LSSE voltage for a GdIG/Pt system at  $T_{\text{sign1}} \sim 270$  K and  $T_{\text{sign2}} \sim 75$  K (Figure 7b). The higher one at  $T_{\text{sign1}}$  corresponds to the compensation point  $T_{\text{comp}}$  of GdIG (Figure 7b, subpanel i), at which the  $\text{Gd}^{3+}$  and

$\text{Fe}^{3+}$  sublattice moments reverse in the presence of  $B$ , so does the SSE signal (135). The sign reversal at  $T_{\text{sign}2}$ , by contrast, does not correspond to any changes in magnetic order. Theoretical modelling based on atomistic spin dynamics (ASD) shows that the sign change at  $T_{\text{sign}2}$  can be explained in terms of the  $T$  dependent magnon modes with opposite polarization ( $\alpha$ - and  $\beta$ -modes in **Figure 7c**) and their thermal occupation (135). At the low  $T < T_{\text{sign}2}$ , the positively-polarized almost gapless  $\alpha$ -mode governs the sign of the LSSE in GdIG. As  $T$  increases, the excitation gap for the negatively-polarized  $\beta$ -mode decreases, and the mode is thermally occupied (see **Figure 7c**). For  $T > T_{\text{sign}2}$ , the spin-current contribution from the  $\beta$ -mode may be greater than that from the  $\alpha$ -mode, causing the sign reversal at  $T_{\text{sign}2}$  (135).

In most theories and experiments, YIG has been modeled as a ferromagnet with a single parabolic magnon mode (83). However, due to its large magnetic primitive cell with localized 20  $\text{Fe}^{3+}$  moments, complicated 20 magnon modes exist, in fact. The spectra were recently computed with finite-temperature ASD modelling (83, 136) and measured with inelastic polarized neutron scattering (133) (**Figure 7d, e**). Interestingly, the gap of an optical mode with the negative polarization is comparable to the thermal energy  $k_{\text{B}}T$  at 300 K, which can be occupied at and above room temperature (see the green dashed lines representing  $k_{\text{B}}T$  at 300 K in **Figure 7d, e**). Calculations show that the optical mode reduces the spin pumping and SSE in YIG at room temperature and beyond due to its opposite polarization to the ferromagnetic acoustic mode (83, 133), which may cause a rapid decrease of SSE in YIG above room temperature, faster than the magnetization (50).

Easy-axis AFMs are also a playground to investigate the impact of the magnon polarization on SSEs. In 2020, Li et al. (36, 126) reported AF LSSEs in  $\text{Cr}_2\text{O}_3$  and  $\alpha\text{-Fe}_2\text{O}_3$  (in its easy-axis phase below  $T_{\text{M}}$ ) and found that the sign of the signals below the spin-flop field  $B_{\text{SF}}$  is opposite to that of ferromagnetic SSEs (**Figure 7f**) (119). The result can be interpreted as the spin current from the negatively-polarized AF magnon mode (blue solid lines in **Figure 7a, subpanels ii, iii**), whose excitation gap  $\omega_0$  decreases with  $B$ . In the SF phase  $B > B_{\text{SF}}$ , the signal changes sign, at which the SSE is dominated by the quasiferromagnetic mode having the positive polarization (see **Figure 7f, a, subpanel iii**). They also found that device surface treatment affects the sign reversal behavior (36, 126), which may explain the previously observed AF LSSEs showing the same sign as the ferromagnetic case (142, 143).

## 7. SSE AS PROBE OF MAGNON-PHONON HYBRIDIZATION AND SCATTERING RATE

Recent experiments have revealed that hybridized magnon-phonon excitations induced by magnetoelastic coupling, i.e., magnon polarons (**Figure 8a, b, subpanels iii, iv, v**), are detected via  $B$ -dependent SSE voltages. Interestingly, the magnon-polaron signals contain unique information about relative scattering strengths of magnons and phonons (59, 146).

A high-resolution field scan discerns saw-tooth peak structures in the LSSE for an YIG-film/Pt bilayer at  $B_{\text{TA}} \sim 2.6$  T and  $B_{\text{LA}} \sim 9.3$  T as marked by the blue and red triangles in **Figure 8c**, respectively (59). The SSE anomalies show up when the acoustic magnon mode in YIG shifts upward with external  $B$  such that TA and LA phonon dispersions become tangential at  $B_{\text{TA}}$  and  $B_{\text{LA}}$  (**Figure 8b**). Under these “touching” conditions, the magnon and phonon modes can be coupled over the largest volume in momentum space, leading to the maximal effect of magnon-polaron formation in magnonic spin transport (compare the

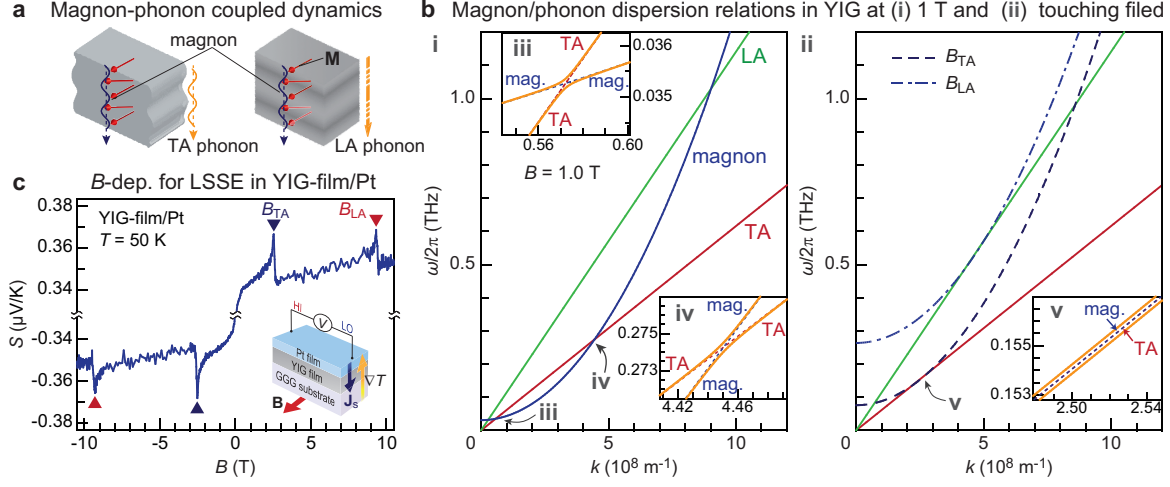


**Figure 8**

(a) Magnon-phonon coupled dynamics. (b) Acoustic magnon, TA-, and LA-phonon dispersion relations in YIG at (i)  $B = 1.0$  T and (ii) the touching field  $B = B_{TA}$  ( $\sim 2.6$  T) and  $B_{LA}$  ( $\sim 9.3$  T). (iii)-(v) Blowups of the hybridized magnon-phonon (TA) modes at (iii, iv)  $B = 1.0$  T and (v)  $B = B_{TA}$ . (c)  $B$  dependence of the LSSE voltage  $S = E_{ISHE}/\nabla T$  for an YIG-film/Pt system (see inset) at  $T = 50$  K. (a),(c) Figure reproduced with permission from Reference (59). Copyright © 2016 American Physical Society.

magnon-phonon (TA) hybridized regions for the “intersect” situation at  $B = 1$  T (**Figure 8b**, subpanels iii, iv) and the “touching” one  $B = B_{TA}$  (**Figure 8b**, subpanel v). The Boltzmann theory (146) revealed that, when the scattering rate of magnons  $\tau_{\text{mag}}^{-1}$  is larger (smaller) than that of phonons  $\tau_{\text{ph}}^{-1}$ , magnon polarons may have a longer (shorter) lifetime than pure magnons and thus enhance (suppress) the SSE at the touching fields. Clear peaks observed in a wide  $T$  range for the YIG film (**Figure 8c**, **Figure 9c**, **g**) suggest higher acoustic than magnetic quality of the sample, i.e.,  $\eta = \tau_{\text{mag}}^{-1}/\tau_{\text{ph}}^{-1} > 1$  (59, 146).

In general, scattering rates for magnons and phonons depend on microscopic scattering mechanism, temperature, wavenumber  $k$ , and sample qualities (146, 147, 151). Indeed, for an YIG-bulk/Pt system, the anomalies take both peak and dip shapes depending on  $T$  and the touching fields  $B_{TA}$  and  $B_{LA}$  (see **Figure 9f**, **h**), showing that  $T$ -,  $k$ -, and  $B$ -dependent magnon and phonon scattering mechanisms should be taken into consideration. Very recently, Shi et al. (151) reported detailed experimental and theoretical studies on magnon-polaron anomalies in YIG-bulk/Pt systems and showed that  $T$ -dependent 4-magnon scattering may lead to dip-to-peak transition (from  $\eta > 1$  to  $\eta < 1$ ).

So far, magnon-polaron anomalies in SSEs have been reported in both the longitudinal and nonlocal configurations for various magnets such as ferrimagnetic YIG (59, 103, 104),  $\text{Fe}_3\text{O}_4$  (148),  $\text{NiFe}_2\text{O}_4$  (108),  $\text{Ni}_{0.65}\text{Zn}_{0.35}\text{Al}_{0.8}\text{Fe}_{1.2}\text{O}_4$  (26), (partially) compensated ferrimagnetic  $\text{Lu}_2\text{Bi}_1\text{Fe}_4\text{Ga}_1\text{O}_{12}$  (22) and  $\text{Gd}_3\text{Fe}_5\text{O}_{12}$  (149), and AF  $\text{Cr}_2\text{O}_3$  (137). The observation of magnon-polaron anomalies in  $\text{Cr}_2\text{O}_3$  below  $B_{SF}$  demonstrates that the SSE in the system is indeed governed by the negatively-polarized magnon mode, opposite to ferromagnetic magnons, giving insight to unraveling the origin of the sign of AF SSEs (127, 150).

It is worthwhile to mention that sufficiently strong magnon-magnon and phonon-phonon

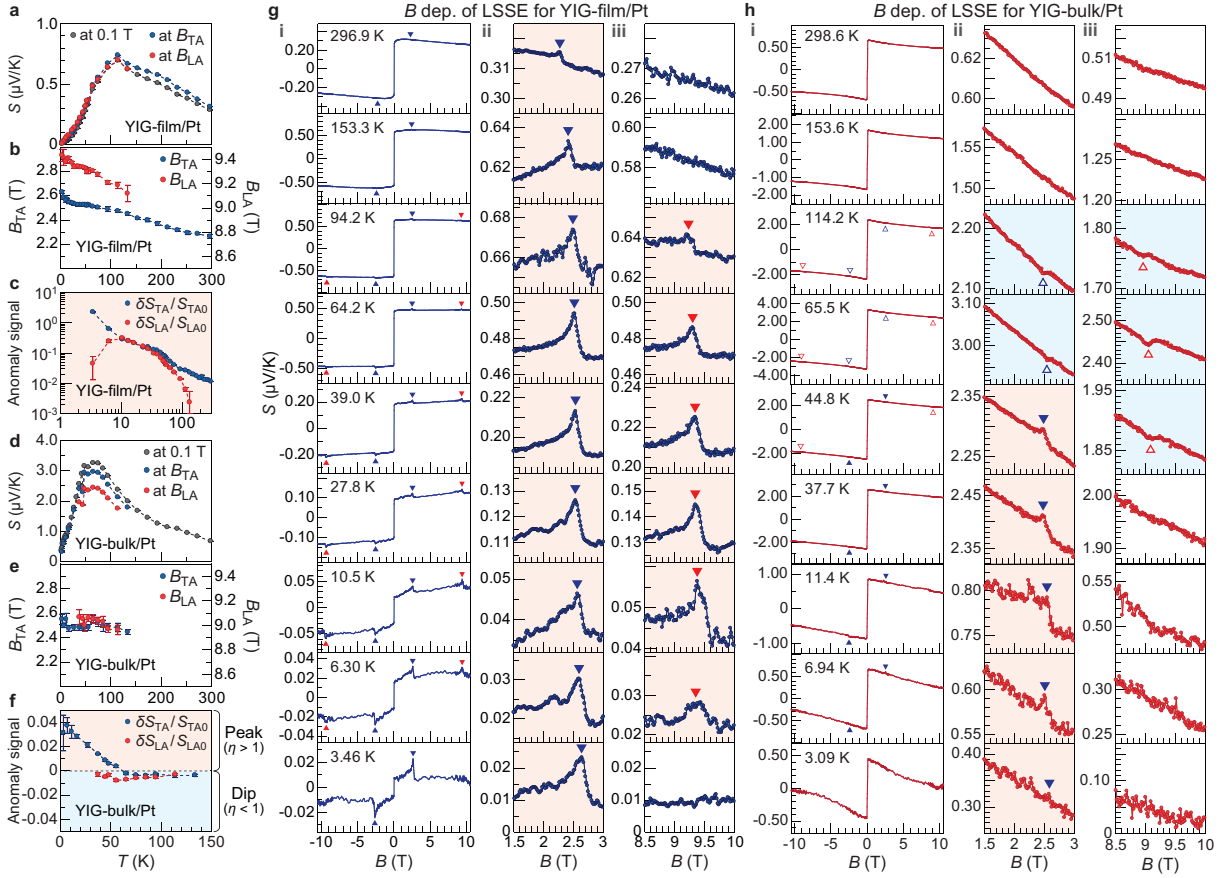


**Figure 9**

(a),(b),(c)  $T$  dependence of the (a) LSSE voltage  $S = E_{\text{ISHE}}/\nabla T$ , (b) anomaly fields  $B_{\text{TA}}$  and  $B_{\text{LA}}$ , and (c) anomaly signal relative to the background one  $\delta S_i/S_{i0} = (S(B_i) - S_{i0})/S_{i0}$  for an YIG-film/Pt system. Here,  $S(B_i)$  and  $S_{i0}$  represent, respectively, the  $S$  and extrapolated background  $S$  intensity at  $B_i$  ( $i = \text{TA}$  or  $\text{LA}$ ) (see Reference (22) for details of the definition of  $\delta S_i/S_{i0}$ ). (d),(e),(f)  $T$  dependence of (d)  $S$ , (e)  $B_{\text{TA}}$  and  $B_{\text{LA}}$ , and (f)  $\delta S_i/S_{i0}$  ( $i = \text{TA}$  or  $\text{LA}$ ) for an YIG-bulk/Pt system. (g),(h)  $B$  dependence of (g,i,h,i)  $S$  for the (g,i) YIG-film/Pt and (h,i) YIG-bulk/Pt at selected  $T$  and blowups of  $S$  around (g,ii,h,ii)  $B_{\text{TA}}$  and (g,iii,h,iii)  $B_{\text{LA}}$ .  $S$  reduction at high  $B$  originates from the freeze-out of magnons by the Zeeman effect (51, 52, 59). The red (blue) shadowed areas show the regions where magnon-polaron peak (dip) signals are observed, indicating  $\eta > 1$  ( $\eta < 1$ ). Data in (a) and (g) below  $T = 50$  K are reproduced with permission from Reference (59). Copyright © 2016 American Physical Society.

scattering processes may destroy the magnon-phonon coherence. Schmidt et al. (152) formulated a Boltzmann transport theory in such a parameter regime and showed that similar SSE anomalies manifest through the “phonon drag” process at the touching fields. In 2021, Schmidt and Brouwer (153) showed a detailed calculation on the low- $T$  LSSE which treats exactly the frequency dependence of the magnon and phonon distribution functions under various scattering mechanisms, beyond the conventional approach based on a Planck-type or Bose-Einstein-type ansatz. They found that, in the low  $T$  below  $\sim 10$  K and in sample sizes relevant to experiments, thermal spin transport in YIG may be dominated by

magnon-polaron modes, which sharply enhances the SSE at the touching field (153).

## 8. SPIN SEEBECK EFFECTS IN QUANTUM MAGNETS

SSE has been studied not only in conventional ferro-, ferri-, and antiferro-magnets, but also in exotic materials called quantum spin liquids (QSLs) with strong quantum fluctuations. Here, QSL in a broader sense is a state of a magnet in which spin correlations are present, while long-range magnetic ordering is absent due to quantum fluctuations reinforced via the low-dimensionality and frustration (46). For such systems, collective excitations of localized spins are no longer conventional spin waves, or magnons, and more exotic spin excitations show up. Recent experiments have revealed that SSE serves as a powerful probe for spin correlation and transport in QSLs, including Tomonaga-Luttinger (TL) spin liquids (45, 46), spin-nematic systems (49), and spin-dimer systems (47, 48).

### 8.1. Spinons in TL spin liquids

Spinons generally refer to magnetic elementary excitations in QSLs (45). The most typical example is found in 1D spin-1/2 chains realized in some oxides such as a Mott insulator  $\text{Sr}_2\text{CuO}_3$  having 1D  $\text{Cu}^{2+}$  spin ( $S = 1/2$ ) with large nearest-neighbor AF exchange coupling  $J_{\parallel}$  ( $\sim 2000$  K, much stronger than the inter-chain coupling  $J_{\perp}$ ; **Figure 10a**) (45). Due to the 1D nature, its spin fluctuation is so strong, leading to a paramagnetic state with strong spin-singlet correlations. The spin excitation from this correlated ground state is particle-like, called a “spinon”, and has a gapless dispersion robust to external fields and magnetic anisotropies (**Figure 10b**).

In 2017, Hirobe et al. (45) demonstrated the spinon SSE in a 1D TL spin liquid state in  $\text{Sr}_2\text{CuO}_3$  with Pt contact. The  $T$  and crystallographic orientation dependencies indicate that the observed LSSE originates from the 1D spin correlation along the chain (**Figure 10c**). The polarity of the signal is opposite to that due to ferromagnetic SSEs, showing that classical spin fluctuations are not responsible for the experimental results. The results were reproduced by adopting the Bethe ansatz into a general formulation of SSE (45), showing that the signal polarity is determined by finite-temperature dynamics of 1D spinons.

### 8.2. Triplons in dimerized spin systems

Among quantum spin systems without magnetic order, dimerized spin systems are an important playground, in which two neighboring spins with AF coupling are frozen as  $S = 0$  singlets in the ground state  $[(|\uparrow\downarrow\rangle - |\downarrow\uparrow\rangle)/\sqrt{2}]$ . The elementary spin excitations are  $S = 1$  triplet states  $[|\downarrow\downarrow\rangle, (|\uparrow\downarrow\rangle + |\downarrow\uparrow\rangle)/\sqrt{2}, \text{ and } |\uparrow\uparrow\rangle]$ , called a “triplon” (**Figure 10d**) (47).

Recently, Chen et al. (47) demonstrated the triplon SSE in a spin-Peierls (SP) material  $\text{CuGeO}_3$  having a 1D  $\text{Cu}^{2+}$  spin-1/2 chains with AF exchange interaction for nearest-neighbor spins. Below its SP transition temperature  $T_{\text{SP}} \sim 14.5$  K, the chain distorts so that the distance between neighboring spins alternates. The bond-alternating exchange interaction causes neighboring spins to dimerize to reduce the total energy, creating a gap in the excitation spectrum ( $\omega_0 \sim 23$  K) (see the triplon dispersions sketched in **Figure 10e**) (47). The triplon states are threefold degenerated at  $B = 0$ , whereas they are lifted to split into three different energy levels under  $B \neq 0$ , the lowest mode of which is the  $|\uparrow\uparrow\rangle$  state carrying a spin polarization opposite to ferromagnetic magnons (same sign as spinons) (45, 46). Chen et al. (47) successfully observed the triplon LSSE in  $\text{CuGeO}_3/\text{Pt}$  systems

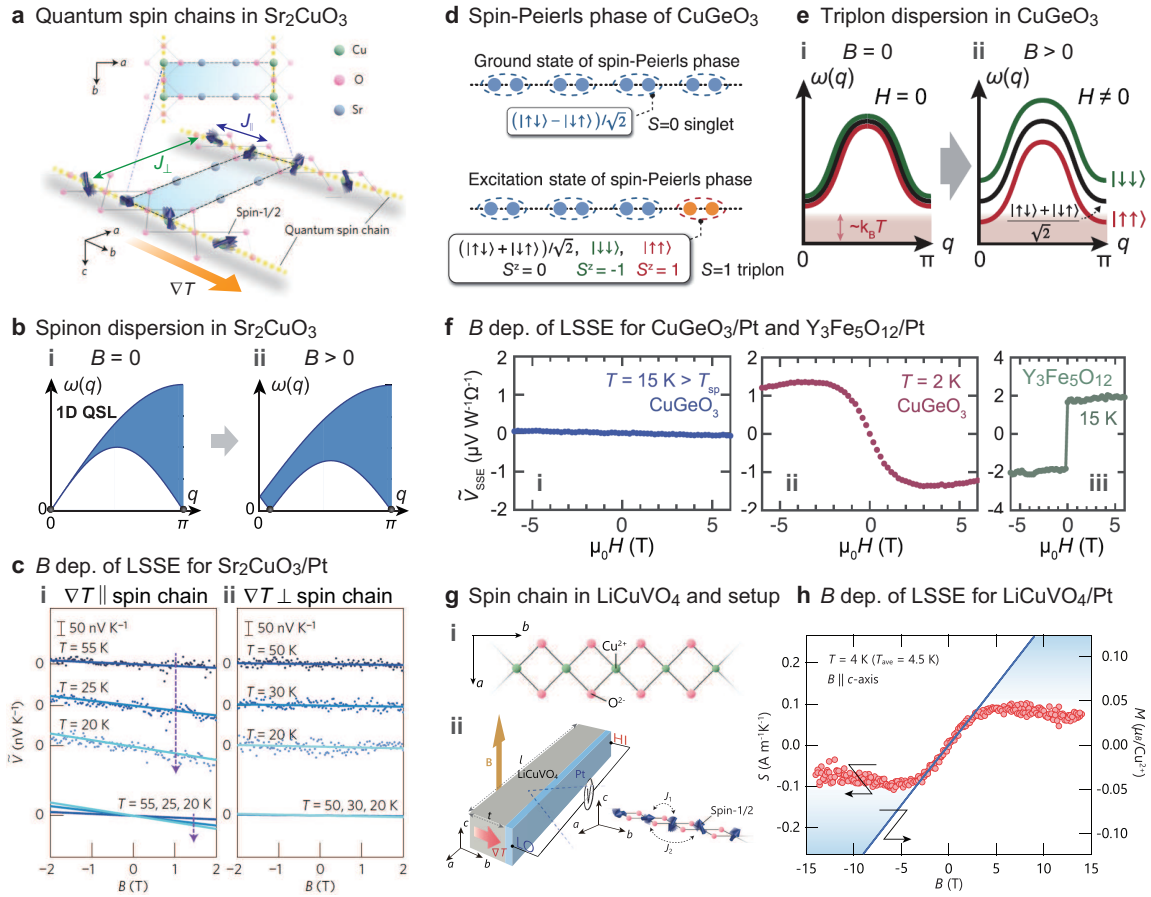


**Figure 10**

(a) Quantum spin chains in  $\text{Sr}_2\text{CuO}_3$  (45). (b) Excitation spectrum,  $\omega(q)$ , of 1D spinons in  $\text{Sr}_2\text{CuO}_3$  under (i) zero and (ii) finite  $B$  (46). Figure reproduced with permission from Reference (46). Copyright © 2018 AIP Publishing. (c)  $B$  dependence of the LSSE voltage  $\tilde{V} = V/\Delta T$  for  $\text{Sr}_2\text{CuO}_3/\text{Pt}$  systems at selected  $T$  for (i)  $\nabla T \parallel$  spin chain and (ii)  $\nabla T \perp$  spin chain (45). (a),(c) Figure reproduced with permission from Reference (45). Copyright © 2016 Springer Nature. (d) Ground and excited states of the spin-Peierls (SP) phase of  $\text{CuGeO}_3$ . (e)  $\omega(q)$  of triplons in  $\text{CuGeO}_3$  under (i) zero and (ii) finite  $B$  (47). (f)  $B$  dependence of the LSSE voltage  $\tilde{V}_{\text{SSE}}$  (the voltage  $V$  normalized by the applied heating power  $P$  and Pt resistance  $R_{\text{Pt}}$ ) for a  $\text{CuGeO}_3/\text{Pt}$  system at (i)  $T = 15 \text{ K} > T_{\text{sp}}$  and (ii)  $2 \text{ K}$  and (iii) for a  $\text{Y}_3\text{Fe}_5\text{O}_{12}/\text{Pt}$  system at  $15 \text{ K}$  (47). (d)-(f) Figure reproduced with permission from Reference (47). Copyright © 2021 Authors, licensed under a Creative Commons Attribution (CC BY) license. (g) (i) Spin chain in  $\text{LiCuVO}_4$  and (ii) Setup for detecting the LSSE in a  $\text{LiCuVO}_4/\text{Pt}$  system. (h)  $B$  dependence of the LSSE voltage  $\tilde{S} = E_{\text{ISHE}}/(\rho_{\text{Pt}}\nabla T)$  ( $\rho_{\text{Pt}}$ : Pt resistivity) for a  $\text{LiCuVO}_4/\text{Pt}$  system and  $M$  in  $\text{LiCuVO}_4$  at  $T = 4 \text{ K}$ . (g),(h) Figure reproduced with permission from Reference (49). Copyright © 2019 American Physical Society.

in the SP phase, whose sign is opposite to that for  $\text{YIG}/\text{Pt}$  as expected (Figure 10f). In 2022, Xing et al. (48) reported the LSSE in a spin-gapped quantum magnet  $\text{Pb}_2\text{V}_3\text{O}_9$  having a relatively low critical field  $B_c$  to form the Bose-Einstein condensation (BEC) states of triplons, at which the excitation gap for  $|\uparrow\uparrow\rangle$  is lower than the energy of ground state (47, 48). They (48) found that the LSSE voltages in  $\text{Pb}_2\text{V}_3\text{O}_9/\text{Pt}$  are maximal at  $B_c$ , whose  $T$  dependence follows the power law for the BEC phase boundary:  $T \propto (B - B_c)^{2/3}$

(48).

### 8.3. Spin-nematic TL liquids

A spin-nematic ordered phase is a physical state with a spin quadrupolar order and without any spin-dipolar (magnetic) order (154). The state typically emerges in a 1D frustrated spin-1/2 chain with the ferromagnetic nearest neighboring exchange interaction  $J_1 < 0$  and the AF next nearest neighboring one  $J_2 > 0$  (Figure 10g) (49). As  $B$  is increased in this system, the spin-nematic TL liquid state appears in a wide  $B$  range. Here, not only single magnons but also magnon pairs (molecules of two magnons) are excited, whose energy gap is equivalent to the binding energy of magnon pairs and zero, respectively.

Hirobe et al. (49) investigated the LSSE in a spin-nematic magnet  $\text{LiCuVO}_4$  with quasi-1D  $\text{Cu}^{2+}$  spin-1/2 chains and observed a strong  $B$ -induced signal reduction (Figure 10h). They attributed the result to the suppressed interfacial spin exchange due to the stabilization of magnon-pairs carrying spin-2 which cannot contribute to the interfacial spin injection in SSE governed by the spin-1 exchange between single magnons and conduction electrons (49) (see Figure 2b). The selective probing feature of spin-1 magnetic excitations for SSEs is distinct from thermal conductivity measurements, as the latter simultaneously probes phonons as well as multiple spin-1 and spin-2 excitations. This study shows that SSE may detect signatures of spin-nematic states and their transport properties (49).

## 9. NUCLEAR-SPIN SEEBECK EFFECT

So far, we have discussed the SSEs caused by electron spins. At low temperatures or high magnetic fields, their efficiency inevitably disappears due to freeze-out of magnons (51, 58). In solids, however, there is an as-yet-unexplored entropy carrier thermally activated even in such an environment: a nuclear spin (Figure 11a). The feature originates from the tiny gyromagnetic ratio of a nuclear spin  $\gamma_n$ ,  $\sim 10^3$  times less than that of an electron  $\gamma$ , which makes its excitation gap in the range below 1 GHz ( $\sim 50$  mK in units of  $T$ ) in ambient fields. Here a question arises: Is it possible that nuclear spins drive SSEs? Based on the ISHE measurements for  $\text{MnCO}_3/\text{Pt}$  systems at ultralow temperatures, we recently answered this question affirmatively (38).

$\text{MnCO}_3$  is an easy-plane canted AF insulator having a large nuclear spin  $I = 5/2$  of  $^{55}\text{Mn}$  nuclei and strong hyperfine coupling (155). Below  $T_N = 35$  K, the  $\text{Mn}^{2+}$  sublattice magnetizations  $\mathbf{M}_1$  and  $\mathbf{M}_2$  are aligned in the (111) plane and canted slightly from the collinear AF configuration due to the Dzyaloshinskii–Moriya interaction (see Figure 11b). The hyperfine (Overhauser) fields  $B_{\text{hf}}$  acting on the  $^{55}\text{Mn}$  sublattice nuclear spins  $\mathbf{I}_1$  and  $\mathbf{I}_2$  from  $\mathbf{M}_1$  and  $\mathbf{M}_2$  reach as large as  $\sim 60$  T (155), which reinforces the nuclear spin polarization ( $\sim 40\%$  at 100 mK) and orients  $\mathbf{I}_1$  and  $\mathbf{I}_2$  along the  $\mathbf{M}_1$  and  $\mathbf{M}_2$  directions, respectively (Figure 11b). Moreover, the canting angle  $\theta$  increases with  $B$ , so does the net nuclear-spin polarization ( $\mathbf{I}_1 + \mathbf{I}_2$ ) along  $\mathbf{B}$ . The advantage makes the nuclear SSE experimentally feasible. Figure 11d shows the  $B$  dependence of the LSSE voltage in  $\text{MnCO}_3/\text{Pt}$  systems for  $100 \text{ mK} < T < 50 \text{ K}$ . The observed SSE is enhanced down to 100 mK and is not suppressed under the strong field of 14 T (see also Figure 11c). Importantly, even in this extreme environment, the nuclear-spin mode in  $\text{MnCO}_3$  can be greatly excited because its excitation gap is as small as  $\sim 30$  mK, which is little affected by the field. By contrast, electronic magnons freeze out by the Zeeman gap  $\gamma B \sim 19$  K, much higher than the thermal

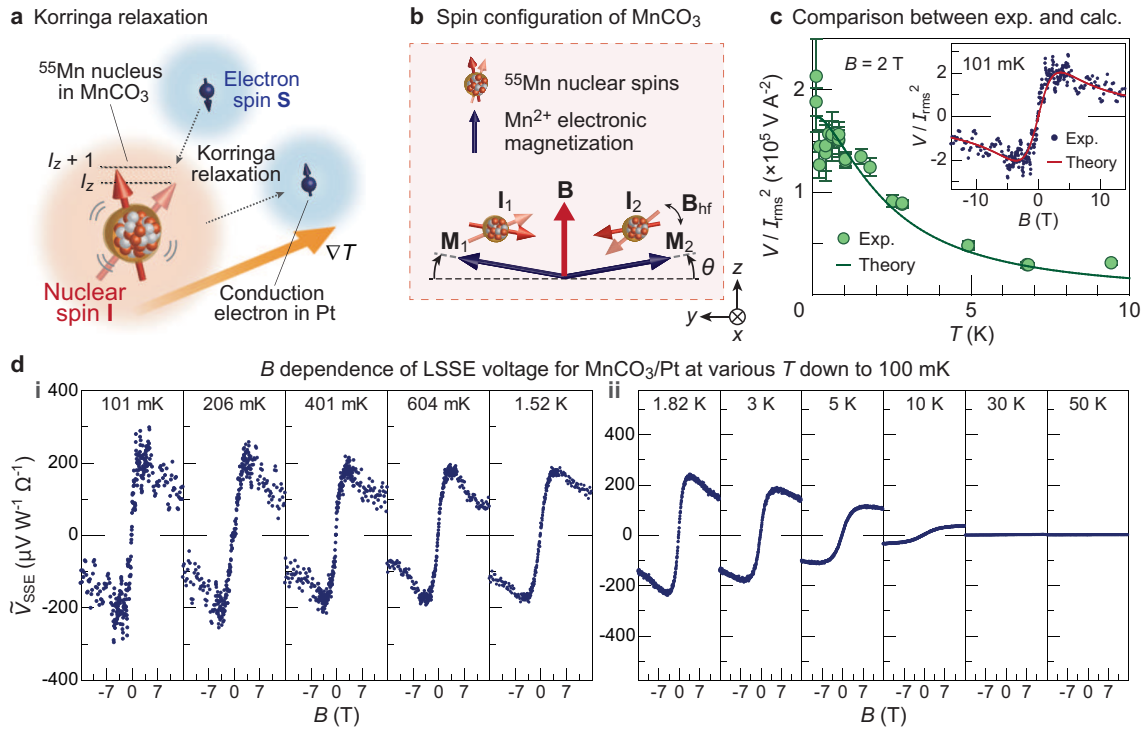


**Figure 11**

(a) Nuclear SSE induced by the interfacial Korrington relaxation process, the spin-conserving flip-flop scattering between a nuclear spin,  $I$ , of  $^{55}\text{Mn}$  in  $\text{MnCO}_3$  and an electron spin,  $S$ , in Pt via the interfacial hyperfine interaction. (b) Orientation of the canted  $\text{Mn}^{2+}$  sublattice magnetizations  $M_1$  and  $M_2$  and the  $^{55}\text{Mn}$  nuclear spins  $I_1$  and  $I_2$  in  $\text{MnCO}_3$  for  $\mathbf{B} \parallel (111)$ . Due to the strong internal hyperfine field of  $B_{\text{hf}} \sim 60$  T,  $I_1$  and  $I_2$  orient (antiparallel) to the  $M_1$  and  $M_2$  directions, respectively. (c)  $T$  dependence of the LSSE voltage  $V$  normalized by the applied current squared  $I_{\text{rms}}^2$  (proportional to the heating power  $P$ ) for  $\text{MnCO}_3/\text{Pt}$  Device 1 at  $B = 2$  T. The inset shows the  $B$  dependence of  $V/I_{\text{rms}}^2$  at  $T = 101$  mK. Theoretical results for the nuclear SSE are also plotted with solid curves. (a)-(c) Figure reproduced from Reference (38). Copyright © 2021 Authors, licensed under a Creative Commons Attribution (CC BY) license. (d)  $B$  dependence of the LSSE voltage  $\tilde{V}_{\text{SSE}} = V_{\text{SHE}}/(PR_{\text{Pt}})$  for (i) Device 1 for  $100 \text{ mK} < T < 1.6 \text{ K}$  and (ii) Device 2 for  $1.8 \text{ K} < T < 50 \text{ K}$ .

energy. A nuclear SSE theory indeed quantitatively reproduces the experimental results, in which interfacial hyperfine coupling between nuclear spins in  $\text{MnCO}_3$  and electrons in Pt is taken into account (38) (see Figure 11a, c).

## 10. SUMMARY AND OUTLOOK

In this article, we reviewed the recent progress of SSE research and discussed its emerging role as an instrument for magnon (phonon) excitations, transport, spin correlation, interfacial spin-exchange, static magnetic and Néel order, and domains. This unique feature is realized because both the interfacial spin-current injection and bulk spin transport play essential roles in SSEs, unlike other conventional spintronic phenomena that appear only in a nanoscale, highlighting the power of SSEs.

There are some interesting theoretical proposals relevant to the present topics. Matsuo

et al. (156) calculate the spin-current noise in spin pumping and SSE, which can be used to determine the effective spin carried by a magnon modified by interfacial spin-nonconserving processes and also to estimate  $\theta_{\text{SH}}$ . Nasu and Naka (157) investigate SSEs in nonmagnetic excitonic insulators (NEIs) and conclude that SSE signals appear without external fields due to the time-reversal symmetry breaking inherent in the NEI state. Takikawa et al. (158) calculate a thermal spin current in a Kitaev spin liquid state and show that the SSE can be a measure of a chiral Majorana edge mode. Besides, magnon polarons discussed in this article may affect magnonic spin and thermal conductivities (146) and also, in the nonlocal configuration, induce a Fulde-Ferrell-Larkin-Ovchinnikov (FFLO)-like oscillatory voltage as a function of injector-detector distance (159). All these theoretical works await experimental demonstration.

Machine learning is becoming a valuable tool to uncover hidden, complicated regularities in datasets. In 2019, Iwasaki et al. (21) demonstrated the utility of machine learning to elucidate the fundamental physics of SSE and optimize key material parameters to enhance the thermopower. Subsequently, they also developed interpretable machine learning (160), which indeed led to the discovery of a material with large spin-driven thermoelectric efficiency. A machine learning-based approach may therefore help not only in developing novel materials, but also in guiding theoretical studies in this field.

Exploitation of SSEs in 2D van der Waals materials with tunable static and dynamical magnetic properties (161, 162) is a fruitful avenue of investigation. Some experiments have been reported recently aside from the LSSEs in  $\text{Cr}_2\text{Si}_2\text{Te}_6$  and  $\text{Cr}_2\text{Ge}_2\text{Te}_6$  (16) discussed in Section 5. In 2019, Xing et al. (115) demonstrated long-distance magnon transport in a quasi-2D AF insulator  $\text{MnPS}_3$  via a nonlocal SSE. Subsequently, the nonlocal SSE in this system is shown to be turned on and off by an electrical current through a metal gate due to the nonlinear gate dependence (116). In 2020, Lee et al. (163) showed that the insertion of a monolayer  $\text{WSe}_2$  between YIG and Pt layers enhances the LSSE voltage by a factor of  $\sim 5$  compared to that in an YIG/Pt system, showing a new avenue on SSE research with 2D transition dichalcogenide materials. In the same year, Liu et al. (117) demonstrated the nonlocal SSE in a 2D ferromagnetic  $\text{CrBr}_3$  flake ( $\sim 10$  layers) fully encapsulated by two layers of h-BN, which paves the way for future magnonic devices (164) with air-sensitive 2D magnets. Studies on SSEs with 2D materials have just begun, and more fascinating phenomena are to be observed through control of the layer number and stacking combinations of 2D materials in the near future.

## DISCLOSURE STATEMENT

The authors are not aware of any affiliations, memberships, funding, or financial holdings that might be perceived as affecting the objectivity of this review.

## ACKNOWLEDGMENTS

The authors thank many colleagues and collaborators for fruitful discussions. This work was supported by JST-CREST (JPMJCR20C1 and JPMJCR20T2), Grant-in-Aid for Scientific Research (JP19H05600 and JP20H02599) from JSPS KAKENHI, Japan, Institute for AI and Beyond of the University of Tokyo, IBM-UTokyo lab, and Daikin Industries, Ltd.

## LITERATURE CITED

1. Uchida K, Ishida M, Kikkawa T, Kirihara A, Murakami T, Saitoh E. 2014. *J. Phys.: Condens. Matter* 26:343202, *ibid.* 26:389601
2. Uchida K, Adachi H, Kikkawa T, Kirihara A, Ishida M, et al. 2016. *Proc. IEEE* 104:1946–1973, *ibid.* 104:1499
3. Uchida K, Takahashi S, Harii K, Ieda J, Koshibae W, et al. 2008. *Nature* 455:778–781
4. Uchida K, Xiao J, Adachi H, Ohe J, Takahashi S, et al. 2010. *Nat. Mater.* 9:894–897
5. Jaworski CM, Yang J, Mack S, Awschalom DD, Heremans JP, Myers RC. 2010. *Nat. Mater.* 9:898–903
6. Uchida K, Adachi H, Ota T, Nakayama H, Maekawa S, Saitoh E. 2010. *Appl. Phys. Lett.* 97:172505.
7. Cornelissen LJ, Liu J, Duine RA, Ben Youssef J, van Wees BJ. 2015. *Nat. Phys.* 11:1022–1026
8. Bauer GEW, Saitoh E, van Wees BJ. 2012. *Nat. Mater.* 11:391–399
9. Boona SR, Myers RC, Heremans JP. 2014. *Energy Environ. Sci.* 7:885–910
10. Yu H, Brechet SD, Ansermet J-P. 2017. *Phys. Lett. A* 381:825–837
11. Maekawa S, Saitoh E, Valenzuela SO, Kimura T, eds. 2017. *Spin Current*. Oxford: Oxford University Press. 2nd Ed.
12. Kikkawa T, Uchida K, Daimon S, Shiomi Y, Adachi H, et al. 2013. *Phys. Rev. B* 88:214403
13. Bougiatioti P, Klewe C, Meier C, Manos O, Kuschel O, et al. 2017. *Phys. Rev. Lett.* 119:227205
14. De A, Ghosh A, Mandal R, Ogale S, Nair S. 2020. *Phys. Rev. Lett.* 124:017203
15. Mallick K, Wagh AA, Ionescu A, Barnes CHW, Anil Kumar PS. 2019. *Phys. Rev. B* 100:224403
16. Ito N, Kikkawa T, Barker J, Hirobe D, Shiomi Y, Saitoh E. 2019. *Phys. Rev. B* 100:060402(R)
17. Gupta V, Cham TM, Stiehl GM, Bose A, Mittelstaedt JA, et al. 2020. *Nano Lett.* 20:7482–7488
18. Cramer J, Guo E-J, Geprägs S, Kehlberger A, Ivanov YP, et al. 2017. *Nano Lett.* 17:3334–3340
19. Avci CO, Quindeau A, Mann M, Pai C-F, Ross CA, Beach GSD. 2017. *Phys. Rev. B* 95:115428
20. Ortiz VH, Gomez MJ, Liu Y, Aldosary M, Shi J, Wilson RB. 2021. *Phys. Rev. Mater.* 5:074401
21. Iwasaki Y, Takeuchi I, Stanev V, Kusne AG, Ishida M, et al. 2019. *Sci. Rep.* 9:2751
22. Ramos R, Hioki T, Hashimoto Y, Kikkawa T, Frey P, et al. 2019. *Nat. Commun.* 10:5162
23. Arboleda JD, Olmos OA, Aguirre MH, Ramos R, Anadon A, Ibarra MR. 2016. *Appl. Phys. Lett.* 108:232401
24. Jiménez-Cavero P, Lucas I, Anadón AA, Ramos R, Niizeki T, et al. 2017. *APL Mater.* 5:026103
25. Shiomi Y, Lustikova J, Saitoh E. 2017. *Sci. Rep.* 7:5358
26. Wang H, Hou D, Kikkawa T, Ramos R, Shen K, et al. 2018. *Appl. Phys. Lett.* 112:142406
27. Kosaki H, Umeda M, Saitoh E, Shiomi Y. 2021. *J. Phys. Soc. Jpn.* 90:083702
28. Hirschner J, Maryško M, Hejtmánek J, Uhrecký R, Soroka M, et al. 2017. *Phys. Rev. B* 96:064428
29. Knížek K, Pashchenko M, Levinský P, Kaman O, Houdková J, et al. 2018. *J. Appl. Phys.* 124:213904
30. Oh I, Park J, Choe D, Jo J, Jeong H, et al. 2021. *Nat. Commun.* 12:1057
31. Holanda J, Maior DS, Alves Santos O, Vilela-Leão LH, Mendes JBS, et al. 2017. *Appl. Phys. Lett.* 111:172405
32. Ribeiro PRT, Machado FLA, Gamino M, Azevedo A, Rezende SM. 2019. *Phys. Rev. B* 99:094432
33. Gray I, Moriyama T, Sivadas N, Stiehl GM, Heron JT, et al. 2019. *Phys. Rev. X* 9:041016
34. Hooeboom GR, van Wees BJ. 2020. *Phys. Rev. B* 102: 214415
35. Li J, Shi Z, Ortiz VH, Aldosary M, Chen C, et al. 2019. *Phys. Rev. Lett.* 122:217204
36. Yuan W, Li J, Shi J. 2020. *Appl. Phys. Lett.* 117:100501
37. Ross A, Lebrun R, Evers M, Deák A, Szunyogh L, et al. 2021. *Phys. Rev. B* 103:224433
38. Kikkawa T, Reitz D, Ito H, Makiuchi T, Sugimoto T, et al. 2021. *Nat. Commun.* 12:4356
39. Shiomi Y, Takashima R, Okuyama D, Gitgeatpong G, Piyawongwatthana P, et al. 2017. *Phys. Rev. B* 96:180414(R)

40. Hong D, Liu C, Pearson JE, Hoffmann A, Fong DD, Bhattacharya A. 2019. *Appl. Phys. Lett.* 114:242403
41. Das A, Eswara Phanindra V, Watson AJ, Banerjee T. 2021. *Appl. Phys. Lett.* 118:052407
42. Hoogeboom GR, Kuschel T, Bauer GEW, Mostovoy MV, Kimel AV, van Wees BJ. 2021. *Phys. Rev. B* 103:134406
43. Aqeel A, Vlietstra N, Roy A, Mostovoy M, van Wees BJ, Palstra TTM. 2016. *Phys. Rev. B* 94:134418
44. Akopyan A, Prasai N, Trump BA, Marcus GG, McQueen TM, Cohn JL. 2020. *Phys. Rev. B* 101:100407(R)
45. Hirobe D, Sato M, Kawamata T, Shiomi Y, Uchida K, et al. 2017. *Nat. Phys.* 13:30–34
46. Hirobe D, Kawamata T, Oyanagi K, Koike Y, Saitoh E. 2018. *J. Appl. Phys.* 123:123903
47. Chen Y, Sato M, Tang Y, Shiomi Y, Oyanagi K, et al. 2021. *Nat. Commun.* 12:5199
48. Xing W, Cai R, Moriyama K, Nara K, Yao Y, et al. 2022. *Appl. Phys. Lett.* 120:042402
49. Hirobe D, Sato M, Hagihala M, Shiomi Y, Masuda T, Saitoh E. 2019. *Phys. Rev. Lett.* 123:117202
50. Uchida K, Kikkawa T, Miura A, Shiomi J, Saitoh E. 2014. *Phys. Rev. X* 4:041023
51. Kikkawa T, Uchida K, Daimon S, Qiu Z, Shiomi Y, Saitoh E. 2015. *Phys. Rev. B* 92:064413
52. Jin H, Boona SR, Yang Z, Myers RC, Heremans JP. 2015. *Phys. Rev. B* 92:054436
53. Guo E-J, Cramer J, Kehlberger A, Ferguson CA, MacLaren DA, et al. 2016. *Phys. Rev. X* 6:031012
54. Iguchi R, Uchida K, Daimon S, Saitoh E. 2017. *Phys. Rev. B* 95:174401
55. Weiler M, Althammer M, Czeschka FD, Huebl H, Wagner MS, et al. 2012. *Phys. Rev. Lett.* 108:106602
56. Aqeel A, Vera-Marun IJ, van Wees BJ, Palstra TTM. 2014. *J. Appl. Phys.* 116:153705
57. Uchida K, Ohe J, Kikkawa T, Daimon S, Hou D, et al. 2015. *Phys. Rev. B* 92:014415
58. Kikkawa T, Uchida K, Daimon S, Saitoh E. 2016. *J. Phys. Soc. Jpn.* 85:065003
59. Kikkawa T, Shen K, Flebus B, Duine RA, Uchida K, et al. 2016. *Phys. Rev. Lett.* 117:207203
60. Kalappattil V, Das R, Phan M-H, Srikanth H. 2017. *Sci. Rep.* 7:13316
61. Wu P-H, Chan Y-T, Hung T-C, Zhang Y-H, Qu D, et al. 2020. *Phys. Rev. B* 102:174426
62. Kehlberger A, Ritzmann U, Hinzke D, Guo EJ, Cramer J, et al. 2015. *Phys. Rev. Lett.* 115:096602
63. Miura A, Kikkawa T, Iguchi R, Uchida K, Saitoh E, Shiomi J. 2017. *Phys. Rev. Mater.* 1:014601
64. Prakash A, Flebus B, Brangham J, Yang F, Tserkovnyak Y, Heremans JP. 2018. *Phys. Rev. B* 97:020408(R)
65. Daimon S, Uchida K, Ujiie N, Hattori Y, Tsuboi R, Saitoh E. 2020. *Appl. Phys. Express* 13:103001
66. Wu H, Huang L, Fang C, Yang BS, Wan CH, et al. 2018. *Phys. Rev. Lett.* 120:097205
67. Nozue T, Kikkawa T, Watamura T, Niizeki T, Ramos R, et al. 2018. *Appl. Phys. Lett.* 113:262402
68. Roschewsky N, Schreier M, Kamra A, Schade F, Ganzhorn K, et al. 2014. *Appl. Phys. Lett.* 104:202410
69. Agrawal M, Vasyuchka VI, Serga AA, Kirihara A, Pirro P, et al. 2014. *Phys. Rev. B* 89:224414
70. Kimling J, Choi GM, Brangham JT, Matalla-Wagner T, Huebner T, et al. 2017. *Phys. Rev. Lett.* 118:057201
71. Bartell JM, Jermain CL, Aradhya SV, Brangham JT, Yang F, et al. 2017. *Phys. Rev. Appl.* 7:044004
72. Hioki T, Iguchi R, Qiu Z, Hou D, Uchida K, Saitoh E. 2017. *Appl. Phys. Express* 10:073002
73. Seifert TS, Jaiswal S, Barker J, Weber ST, Razdolski I, et al. 2018. *Nat. Commun.* 9: 2899
74. Jamison JS, Yang Z, Giles BL, Brangham JT, Wu G, et al. 2019. *Phys. Rev. B* 100:134402
75. Flipse J, Dejene FK, Wagenaar D, Bauer GEW, Ben Youssef J, van Wees BJ. 2014. *Phys. Rev. Lett.* 113:027601

76. Daimon S, Iguchi R, Hioki T, Saitoh E, Uchida K. 2016. *Nat. Commun.* 7:13754
77. Sola A, Basso V, Kuepferling M, Dubs C, Pasquale M. 2019. *Sci. Rep.* 9:2047
78. Agrawal M, Vasyuchka VI, Serga AA, Karenowska AD, Melkov GA, Hillebrands B. 2013. *Phys. Rev. Lett.* 111:107204
79. Cornelissen LJ, Peters KJH, Bauer GEW, Duine RA, van Wees BJ. 2016. *Phys. Rev. B* 94:014412
80. An K, Olsson KS, Weathers A, Sullivan S, Chen X, et al. 2016. *Phys. Rev. Lett.* 117:107202
81. Olsson KS, An K, Fiete GA, Zhou J, Shi L, Li X. 2020. *Phys. Rev. X* 10:021029
82. Xiao J, Bauer GEW, Uchida K, Saitoh E, Maekawa S. 2010. *Phys. Rev. B* 81:214418
83. Barker J, Bauer GEW. 2016. *Phys. Rev. Lett.* 117:217201
84. Adachi H, Ohe J, Takahashi S, Maekawa S. 2011. *Phys. Rev. B* 83:094410
85. Adachi H, Uchida K, Saitoh E, Maekawa S. 2013. *Rep. Prog. Phys.* 76:036501
86. Bender SA, Duine RA, Tserkovnyak Y. 2012. *Phys. Rev. Lett.* 108:246601
87. Duine RA, Brataas A, Bender SA, Tserkovnyak Y. 2015. arXiv:1505.01329
88. Zhang SSL, Zhang S. 2012. *Phys. Rev. B* 86:214424
89. Rezende SM, Rodríguez-Suárez RL, Cunha RO, Rodrigues AR, Machado FLA, et al. 2014. *Phys. Rev. B* 89:014416
90. Rezende SM. 2020. *Fundamentals of Magnonics*. Switzerland: Springer Nature Switzerland AG
91. Anadón A, Ramos R, Lucas I, Algarabel PA, Morellón L, et al. 2016. *Appl. Phys. Lett.* 109:012404
92. Venkat G, Cox CDW, Voneshen D, Caruana AJ, Piovano A, et al. 2020. *Phys. Rev. Mater.* 4:075402
93. Ramos R, Kikkawa T, Aguirre MH, Lucas I, Anadón A, et al. 2015. *Phys. Rev. B* 92:220407(R)
94. Cornelissen LJ, Shan J, van Wees BJ. 2016. *Phys. Rev. B* 94:180402(R)
95. Shan J, Cornelissen LJ, Liu J, Ben Youssef J, Liang L, van Wees BJ. 2017. *Phys. Rev. B* 96:184427
96. An K, Kohno R, Thiery N, Reitz D, Vila L, et al. 2021. *Phys. Rev. B* 103:174432
97. Giles BL, Yang Z, Jamison JS, Myers RC. 2015. *Phys. Rev. B* 92:224415
98. Giles BL, Yang Z, Jamison J, Gomez-Perez JM, Vélez S, et al. 2017. *Phys. Rev. B* 96:180412(R)
99. Cornelissen LJ, van Wees BJ. 2016. *Phys. Rev. B* 93:020403(R)
100. Shan J, Cornelissen LJ, Vlietstra N, Ben Youssef J, Kuschel T, et al. 2016. *Phys. Rev. B* 94:174437
101. Zhou XJ, Shi GY, Han JH, Yang QH, Rao YH, et al. 2017. *Appl. Phys. Lett.* 110:062407
102. Ganzhorn K, Wimmer T, Cramer J, Schlitz R, Geprägs S, et al. 2017. *AIP Adv.* 7:085102
103. Cornelissen LJ, Oyanagi K, Kikkawa T, Qiu Z, Kuschel T, et al. 2017. *Phys. Rev. B* 96:104441
104. Oyanagi K, Kikkawa T, Saitoh E. 2020. *AIP Adv.* 10:015031
105. Gomez-Perez JM, Vélez S, Hueso LE, Casanova F. 2020. *Phys. Rev. B* 101:184420
106. Ganzhorn K, Wimmer T, Barker J, Bauer GEW, Qiu Z, et al. 2017. arXiv:1705.02871
107. Avci CO, Rosenberg E, Huang M, Bauer J, Ross CA, Beach GSD. 2020. *Phys. Rev. Lett.* 124:027701
108. Shan J, Singh AV, Liang L, Cornelissen LJ, Galazka Z, et al. 2018. *Appl. Phys. Lett.* 113:162403
109. Li R, Li P, Yi D, Riddiford LJ, Chai Y, et al. 2022. *Nano Lett.* 22:1167–1173
110. Lebrun R, Ross A, Bender SA, Qaiumzadeh A, Baldrati L, et al. 2018. *Nature* 561:222–225
111. Yuan W, Zhu Q, Su T, Yao Y, Xing W, et al. 2018. *Sci. Adv.* 4:eaat1098
112. Muduli P, Schlitz R, Kosub T, Hübner R, Erbe A, et al. 2021. *APL Mater.* 9:021122
113. Das S, Ross A, Ma XX, Becker S, Schmitt C, et al. 2021. arXiv:2112.05947
114. Parsonnet E, Caretta L, Nagarajan V, Zhang H, Taghinejad H, et al. 2022. arXiv:2203.16519
115. Xing W, Qiu L, Wang X, Yao Y, Ma Y, et al. 2019. *Phys. Rev. X* 9:011026
116. Chen G, Qi S, Liu J, Chen D, Wang J, et al. 2021. *Nat. Commun.* 12:6279
117. Liu T, Peiro J, de Wal DK, Leutenantsmeyer JC, Guimarães MHD, van Wees BJ. 2020. *Phys. Rev. B* 101:205407

118. Althammer M. 2020. *Phys. Stat. Solid.* 15:2100130
119. Schreier M, Bauer GEW, Vasyuchka VI, Flipse J, Uchida K, et al. 2015. *J. Phys. D: Appl. Phys.* 48:025001
120. Li Z, Kriefft J, Singh AV, Regmi S, Rastogi A, et al. 2019. *Appl. Phys. Lett.* 114:232404
121. Chanda A, Holzmann C, Schulz N, Seyd J, Albrecht M, et al. 2022. *Adv. Funct. Mater.* 32:21091
122. Sola A, Barton C, Basso V, Dubs C, Pasquale M, Kazakova O. 2020. *Phys. Rev. Applied* 14:034056
123. Yahiro R, Kikkawa T, Ramos R, Oyanagi K, Hioki T, et al. 2020. *Phys. Rev. B* 101:024407
124. Yagmur A, Iguchi R, Geprägs S, Erb A, Daimon S, et al. 2018. *J. Phys. D: Appl. Phys.* 51:194002
125. Qiu Z, Hou D, Barker J, Yamamoto K, Gomony O, Saitoh E. 2018. *Nat. Mat.* 77:577–580
126. Li J, Wilson CB, Cheng R, Lohmann M, Kavand M, et al. 2020. *Nature* 578:70–74
127. Reitz D, Li J, Yuan W, Shi J, Tserkovnyak Y. 2020. *Phys. Rev. B* 102:020408(R)
128. Luo L, Liu C, Saglam H, Li Y, Zhang W, et al. 2021. *Phys. Rev. B* 103:L020401
129. Liu C, Luo L, Hong D, Zhang SSL, Saglam H, et al. 2021. *Sci. Adv.* 7:eabg1669
130. Lin W, Chen K, Zhang S, Chien CL. 2016. *Phys. Rev. Lett.* 116:186601
131. Chen K, Lin W, Chien CL, Zhang S. 2016. *Phys. Rev. B* 94:054413
132. Prakash A, Brangham J, Yang F, Heremans JP. 2016. *Phys. Rev. B* 94:014427
133. Nambu Y, Barker J, Okino Y, Kikkawa T, Shiomi Y, et al. 2020. *Phys. Rev. Lett.* 125:027201
134. Barker J, Atxitia U. 2021. *J. Phys. Soc. Jpn.* 90:081001
135. Geprägs S, Kehlberger A, Coletta FD, Qiu Z, Guo EJ, et al. 2016. *Nat. Commun.* 7:10452
136. Barker J, Bauer GEW. 2019. *Phys. Rev. B* 100:140401(R)
137. Li J, Simensen HT, Reitz D, Sun Q, Yuan W, et al. 2020. *Phys. Rev. Lett.* 25:217201
138. Wu SM, Pearson JE, Bhattacharya A. et al. 2015. *Phys. Rev. Lett.* 114:186602
139. Liu C, Wu SM, Pearson JE, Jiang JS, d’Ambrumenil N, Bhattacharya A. 2018. *Phys. Rev. B* 98:060415(R)
140. Oyanagi K, Takahashi S, Cornelissen LJ, Shan J, Daimon S, et al. 2019. *Nat. Commun.* 10:4740
141. Yamamoto Y, Ichioka M, Adachi H. 2019. *Phys. Rev. B* 100:064419
142. Seki S, Ideue T, Kubota M, Kozuka Y, Takagi R, et al. 2015. *Phys. Rev. Lett.* 115:266601
143. Wu SM, Zhang W, KC A, Borisov P, Pearson JE, et al. 2016. *Phys. Rev. Lett.* 116:097204
144. Williams TJ, Aczel AA, Lumsden MD, Nagler SE. 2015. *Phys. Rev. B* 92:144404
145. Spachmann S, Elghandour A, Selter S, Büchner B, Aswartham S, Klingeler R. 2022. arXiv:2202.03251
146. Flebus B, Shen K, Kikkawa T, Uchida K, Qiu Z, et al. 2017. *Phys. Rev. B* 95:144420
147. Streib S, Vidal-Silva N, Shen K, Bauer GEW. 2019. *Phys. Rev. B* 99:184442
148. Xing W, Ma Y, Yao Y, Cai R, Ji Y, et al. 2020. *Phys. Rev. B* 102:184416
149. Yang B, Xia SY, Zhao H, Liu G, Du J, et al. 2021. *Phys. Rev. B* 103:054411
150. Yamamoto Y, Ichioka M, Adachi H. 2022. *Phys. Rev. B* 105:104417
151. Shi Z, Xi Q, Li J, Li Y, Aldosary M, et al. 2021. *Phys. Rev. Lett.* 127:277203
152. Schmidt R, Wilken F, Nunner TS, Brouwer PW. 2018. *Phys. Rev. B* 98:134421
153. Schmidt R, Brouwer PW. 2021. *Phys. Rev. B* 103:014412
154. Sato M, Morisaku Y. 2020. *Phys. Rev. B* 102:060401(R)
155. Shiomi Y, Lustikova J, Watanabe S, Hirobe D, Takahashi S, Saitoh E. 2019. *Nat. Phys.* 15:22–26
156. Matsuo M, Ohnuma Y, Kato T, Maekawa S. 2018. *Phys. Rev. Lett.* 120:037201
157. Nasu J, Naka M. 2021. *Phys. Rev. B* 103:L121104
158. Takikawa D, Yamada MG, Fujimoto S. 2022. *Phys. Rev. B* 105:115137
159. Rameshti BZ, Duine RA. 2019. *Phys. Rev. B* 99:060402(R)
160. Iwasaki Y, Sawada R, Stanev V, Ishida M, Kirihara A, et al. 2019. *npj Comput. Mater.* 5:103
161. Gibertini M, Koperski M, Morpurgo AF, Novoselov KS. 2019. *Nat. Nanotech.* 14:408–419

162. Mak KF, Shan J, Ralph DC. 2019. *Nat. Rev. Phys.* 1:646–661
163. Lee S-K, Lee W-Y, Kikkawa T, Le CT, Kang M-S, et al. 2020. *Adv. Func. Mater.* 30:2003192
164. Chumak AV, Kabos P, Wu M, Abert C, Adelman C, et al. 2022. *IEEE Trans. Magn.* DOI: 10.1109/TMAG.2022.3149664